OBLIQUE IMPACT CRATERING: A COMPARISON OF LOW-VELOCITY EXPERIMENTS TO HIGH-VELOCITY EXPERIMENTS

A

THESIS

Presented to the Faculty

of the University of Alaska Fairbanks

In Partial Fulfillment of the Requirements

for the Degree of

MASTER OF SCIENCE

By

Katie Kristine Hessen, B.S.

Fairbanks, Alaska

December 2008

Abstract

Previous impact cratering experiments performed by Gault and Wedekind (1978), used high-velocity impactors (~1 km/s to 7 km/s) to quantify how impact angle affects crater morphology and ejecta pattern. Low velocity (144 m/s to 260 m/s) impact experiments were conducted in a vacuum chamber with a basaltic sand target material and impact angles ranging from 0.5° to 90° (vertical) at the Impact Cratering Laboratory at the University of Tokyo Kashiwa. The crater morphology and ejecta distribution from low velocity impacts are then compared to results from the higher velocity projectiles. When adjustments are made to the low-velocity measurements to account for differences in velocity, the displaced mass ratio follows a $\sin\theta$ distribution, as is seen in the high-velocity experiments. In the low-velocity experiments, asymmetric ejecta is present at slightly higher impact angles. The presence of an uprange forbidden zone occurs at the same impact angle (20°) in both sets of experiments. The most striking difference between the two sets of experiments is the complete lack of a downrange forbidden zone in all of the low-velocity experiments. With the exception of the very lowest impact angles, these low-velocity oblique impact experiments yield similar changes in crater characteristics with varying impact angles to the previous high-velocity experiments.

Table of Contents

List of Figures

Page

List of Tables

Page

List of Other Materials

1. Introduction

Impact cratering is the most common and widespread geologic process in the solar system. The surfaces of many of the solid bodies in our solar system are dominated by impact craters. Ancient surfaces, like much of Mercury and the lunar highlands, are saturated by craters. Bodies that have experienced resurfacing due to geologic activity have fewer observed craters, like Earth, Mars, and Venus, where the number depends on the time elapsed since the resurfacing event occurred. Planets with substantial atmospheres, like Venus and Titan, have far fewer craters than other bodies because small impactors may ablate, fragment, or be slowed to very low speeds in their atmospheres and never reach the surface or produce a crater. Crater populations are used to determine the age of a particular area or surface on other planets (e.g. Hartmann, 1999), and in inferring their geologic histories and the processes that have affected them. Relative ages of two or more areas on one body can be determined by comparing their crater densities (number of craters per unit area); surfaces with more craters are older. Absolute ages can be estimated if the crater density and the rate of crater formation are known (however, cratering rates outside the Earth-Moon system are not well known).

Impact craters also provide insight into the crustal and atmospheric properties of other planets. Surface material is excavated during the impact process, exposing deeper material that would otherwise not be visible. Pieces of ejecta can also be launched from the surface at speeds exceeding the escape velocity for their parent body, creating the possibility for pieces of one planet to be launched into space and land on another planet.

This is believed to be the origin of the Martian and Lunar meteorites found on Earth (e.g. Melosh, 1985).

Craters formed at lower impact angles are visibly distinguishable from higher angle impacts due to their elongate crater shape and distinctive asymmetric ejecta patterns (Figures 1.1 and 1.2). Impact angles for specific planetary impacts have been inferred (Herrick and Forsberg-Taylor, 2003; Herrick and Hessen, 2006) based on the cumulative fraction of craters with particular features on a planet and the frequency function for the impact angle (Shoemaker, 1962). Understanding how the cratering process changes with impact angle is important because it helps to explain why there is a range in crater morphologies on the planets and allows for estimation of impact angle as stated above. Some studies have been done (with differing conclusions) using the oblique crater population to infer/dispute the possibility of a past population of moonlets that impacted the surface of Mars (Schultz and Lutz-Garihan, 1982; Bottke et al., 2000, Chappelow and Herrick, in press). In addition, the unique ejecta distribution of highly oblique craters can tell about the surface and atmospheric properties of the planet or region where the craters are located (e.g. Barlow and Perez, 2003). For example, comparisons of Venusian, Martian, and lunar oblique impacts highlight the differences in ejecta morphology on bodies with a dense atmosphere, near surface volatiles, and vacuum-like conditions, respectively (Herrick and Forsberg-Taylor, 2003; Herrick and Hessen, 2006; Barlow and Perez, 2003).

The purpose of this project is to conduct experiments and analyze impact craters formed by low-velocity impactors into sand to better define the progression of ejecta

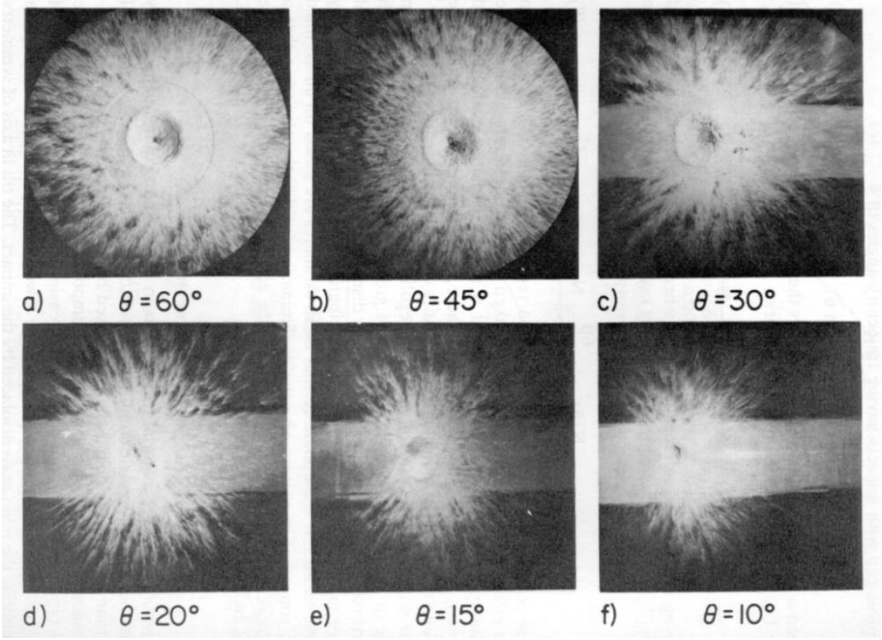

Figure 1.1. Effects of oblique trajectory on distribution of ejecta around craters formed in pumice dust by impacts of pyrex spheres at velocity approximately 6.4 km/s. Trajectories are from left to right, and θ is the impact angle. From Gault and Wedekind (1978), Figure 10.

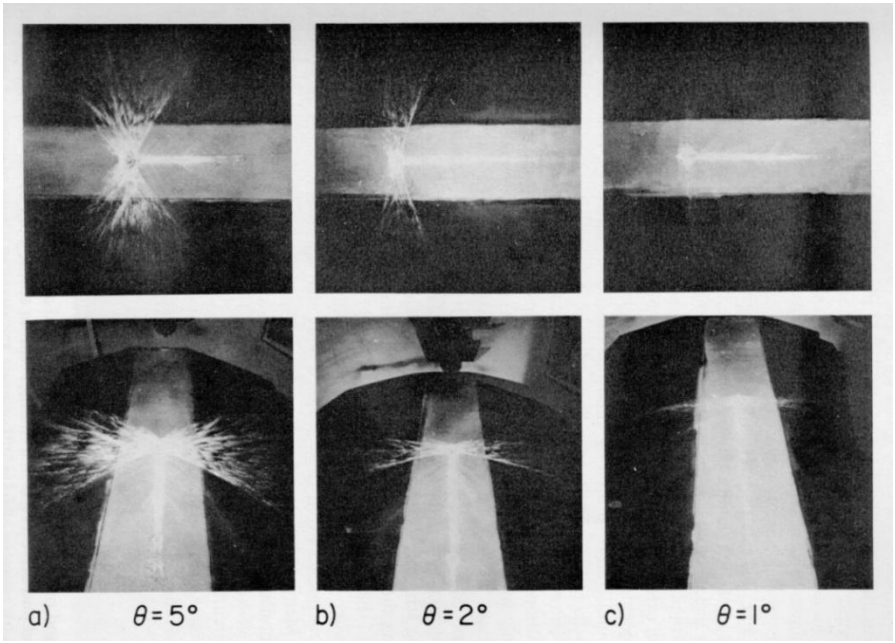

Figure 1.2. Effects of oblique trajectory on distribution of ejecta around craters formed in pumice dust by grazing impacts of pyrex spheres at velocities of approximately 6.4 km/s. Trajectories are from left to right in upper views and from top to bottom in lower views, and θ is the impact angle. From Gault and Wedekind (1978), Figure 11.

distribution and crater shape with varying impact angle. These low velocity craters (144 m/s to 260 m/s) will then be compared to those created at higher velocities (1 km/s to 7 km/s, from Gault and Wedekind, 1978) in order to see if they may be useful in impact studies as a simpler and less expensive substitute for high velocity experiments.

The overall objective of this project is to improve our understanding of oblique impact cratering based on experimental data. This was accomplished by (1) using an experimental setup to create, photograph, and measure a set of laboratory impact craters, (2) investigating impact angle effects on crater shape, and (3) comparing these craters to ones formed at higher velocities.

1.1 Background

The frequency function (probability) dP for impactors approaching from random directions and impacting at zenith angle θ,

$$dP = \sin 2\theta \, d\theta = 2 \sin\theta \cos\theta \, d\theta \qquad (1.1)$$

indicates that half of all impacts occur at incidence angles less than 45° (Shoemaker, 1962). This implies that oblique impacts must constitute a significant fraction of any planetary population of craters. In general, for any given impact angle, there is a certain fraction of any random crater population whose formative events occurred at shallower angles. This fact has been used to define certain impact angles where certain morphological features appear, as impact angle decreases (Herrick and Hessen, 2006; Herrick and Forsberg-Taylor, 2003). This could also be accomplished by direct

experimentation (e. g. Gault and Wedekind, 1978), assuming that laboratory impacts can be scaled to represent the larger planetary craters.

A fundamental problem in impact studies is that most experimental impacts are only a few tens of centimeters across, while most planetary impacts of interest range from a few kilometers to over one thousand kilometers in diameter. This problem is often addressed by using dimensionless ratios to compare small, laboratory-scale craters with larger, planetary craters or with other sets of experiments. One such quantity used is cratering efficiency (denoted as π_v; Melosh, 1989):

$$\pi_V = \frac{M_{crater}}{M_{projectile}}, \quad (1.2)$$

where M_{crater} is the mass of material displaced from the crater and $M_{projectile}$ is the mass of the projectile. Another common quantity used is the mass ratio:

$$\text{Mass ratio} = \frac{M_{crater}}{M_{90^\circ}}, \quad (1.3)$$

where M_{crater} is the mass of material displaced by a crater formed at a given impact angle and M_{90° is the mass displaced by a vertical impact with a similar velocity. These dimensionless ratios are then plotted versus impact angle. Using either of these quantities, rather than non-normalized quantities such as crater diameter or volume, can alleviate some of the problems associated with comparing different sets of impacts.

1.2 Previous Experiments

Gault and Wedekind (1978, from this point on referred to as Gault and Wedekind) conducted a series of experimental impacts in a vacuum to test the effect of varying

impact angle on crater morphology. This study had a wide range of impact velocities, 0.05 km/s to 7.2 km/s, and used three different target materials: quartz sand, pumice powder, and solid granite. In general, they found that craters remain circular as impact angle decreases from vertical, until at least 30°. Below 30°, crater shape becomes a function of target material and projectile properties. For sand and pumice targets, Gault and Wedekind found that all craters become markedly elongate along the path of the projectile below 10°. They also determined that crater diameter decreases with lower impact angles, all other variables remaining constant. To avoid complications with measuring elongate craters, changes in crater dimensions were expressed in terms of the mass of target material displaced (instead of crater diameter). Their experiments also showed that displaced mass (expressed as mass ratio) is approximately proportional to the sine of the impact angle (θ) for impacts into sand and pumice dust (they found a $\sin^2\theta$ relationship for impacts into solid granite).

Gault and Wedekind also closely examined the ejecta distribution as the impact angles became more oblique. Figures 1.1 and 1.2 show the progression of ejecta with impact angle. They found that the ejecta was symmetric in all directions down to approximately 45°. Near 45°, there begins to be visibly less ejecta in the uprange direction. Near 30°, craters have only a small amount of ejecta in the downrange direction as well as the uprange. At around 20°, a clear forbidden zone (an area where no ejecta exists) develops in the uprange direction. Below 20°, decreasing amounts of ejecta are present in the downrange direction until a second forbidden zone develops downrange at approximately 5°. Below 5°, both forbidden zones increase in size, so that only a small

amount of ejecta is present in the crossrange direction (at right angles to the projectile path). Craters exhibiting forbidden zones in both the uprange and downrange directions are termed ‘Butterfly’ craters.

There are many details of crater formation that can be investigated by studying these impact experiments. Unfortunately, the raw data from the experiments of Gault and Wedekind is no longer available. This leaves the scientific community with only the small sampling of their data that was published, much of which is only presented as ‘representative data.’ In particular, it would be valuable to view the complete data set, including videos of crater formation (only a few screenshots are published), higher quality images of the resulting crater and ejecta, and images of their craters formed at slower velocities (the published images are of craters formed at approximately 6 km/s, although their experimental velocities varied from 0.05 to 7.2 km/s).

1.3 Observed Ejecta of Martian Craters

Herrick and Hessen (2006) surveyed ejecta planforms for well-preserved impact craters on Mars with diameters greater than 5 km. The authors classified the craters based on ejecta planform, and identified a progression of ejecta planform change with increasing impact angle. A range of impact angles was inferred for each category of craters based on the percentages of the total crater population and the frequency distribution of Shoemaker (1962) (Equation 1.1). It was noted that the ejecta planforms and the angles at which they occur are very similar to the experiments of Gault and Wedekind (1978). At angles less than ~40°, the ejecta becomes offset in the downrange

direction. At angles less than ~20°, a forbidden zone develops in the uprange direction. At angles less than ~10°, a second forbidden zone develops in the downrange direction, creating a butterfly ejecta pattern (Figure 1.3).

2. Methods

To better understand the oblique impact process, experiments creating impact craters at varying impact angles were conducted using low-velocity projectiles. For ease in comparison with craters from the Moon, Mars, and previous oblique impact studies, and to eliminate interactions between the impact ejecta and an atmosphere, the experiments were conducted in a vacuum chamber with pressures less than 100 Pa. A particulate target material with little or no strength was chosen so that the crater growth process is dominated by gravity (not material strength), as is the case with planetary scale craters. The experimental set-up was designed to allow easy distinction between ejecta and the target surface, so that the distribution of ejecta around the crater could be readily identified for each crater.

2.1 Experimental Procedure

The low-velocity laboratory experiments were completed using the Impact Cratering Laboratory at the Department of Complexity Science, University of Tokyo Kashiwa in the summer of 2005 [see Yamamoto et al. (2006) for reference to the lab facilities]. The experiments were conducted by firing a cylindrical polycarbonate

a. 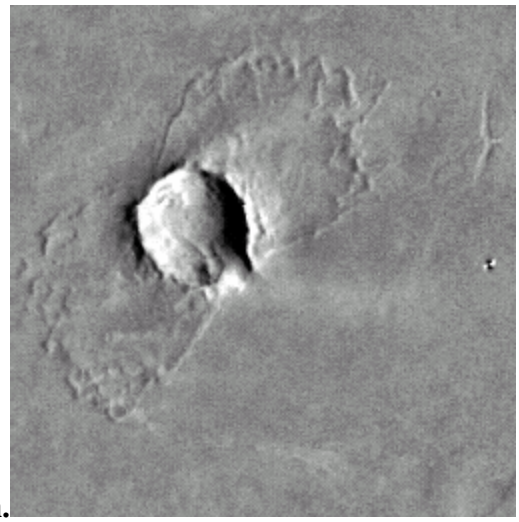 **b.** 

Figure 1.3. Impact craters on Mars. **a.** Oblique impact crater located at 9.2° N, 279.6° E. Maximum crater diameter is 13 km. Crater is elongate and ejecta is concentrated in two lobes on opposite sides of the crater (butterfly ejecta pattern). **b.** Symmetric impact crater located at 35.4°N, 311.2°E. Diameter is 10 km. Crater is circular and ejecta is symmetric about the crater.

projectile (mass 0.49g, length 0.8 cm, diameter 1.0 cm) from a single-stage light-gas gun into a target in a metal chamber capable of near-vacuum pressure conditions. The chamber (Figures 2.1 and 2.2) has ports for mounting the gun at 90° (vertical), 75°, 60°, 45°, 30°, and 15°. The target container was tilted up to 15° to achieve impact angles between the 15° gun port increments. Impact angles ranging from 90° to 0.5° were achieved, producing finer increments in angle than have been published in previous impact studies.

The target was prepared by filling a metal bowl inside the vacuum chamber with brown basaltic sand (grain size less than 500 microns, density 1.44g/cc) and then dusting the sand surface with white flour to make the ejecta easily distinguishable from the target surface. The air was then pumped out of the chamber until the pressure inside was below 100 Pa, after which the polycarbonate projectile was fired from the gun. Projectile velocity was calculated by recording the time it took the projectile to span the 5 centimeter distance between two laser beams inside the barrel. Velocities ranged from 144 m/s to 260 m/s. Each shot was imaged with a digital video recorder at 200 frames per second and digital images were acquired of the resulting crater from various known angles.

Crater depth and rim to rim diameter (Figure 2.3) were measured for most craters by holding a ruler up to the crater. Crater shape was approximated by taking a profile using an apparatus called a profiler (Figure 2.4). It is designed to be positioned above the crater, so that metal pegs can be lowered to the surface of the target/crater with minimal disturbance to the surface. The profiler is then placed on its side, and the profile of the

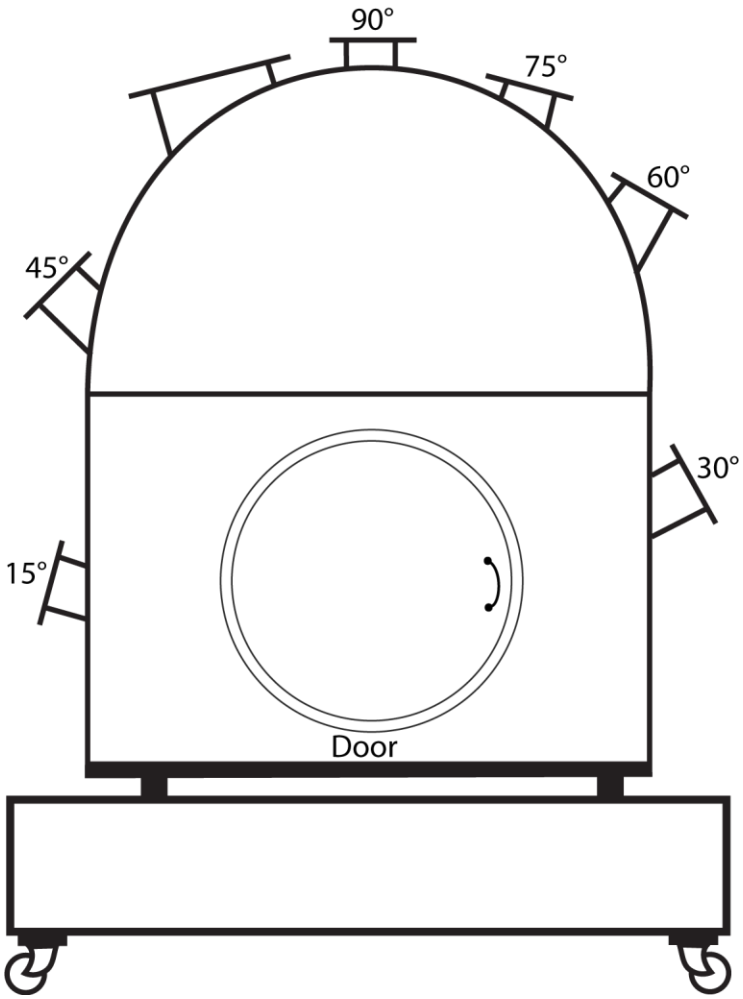

Figure 2.1. Schematic of impact chamber showing the access door and location of ports where the gun can be mounted. Numbers indicate impact angle achieved when gun is mounted on that port, in degrees from horizontal. Chamber is approximately 1.75 meters from the bottom of the wheels to the top of the 90° gun port.

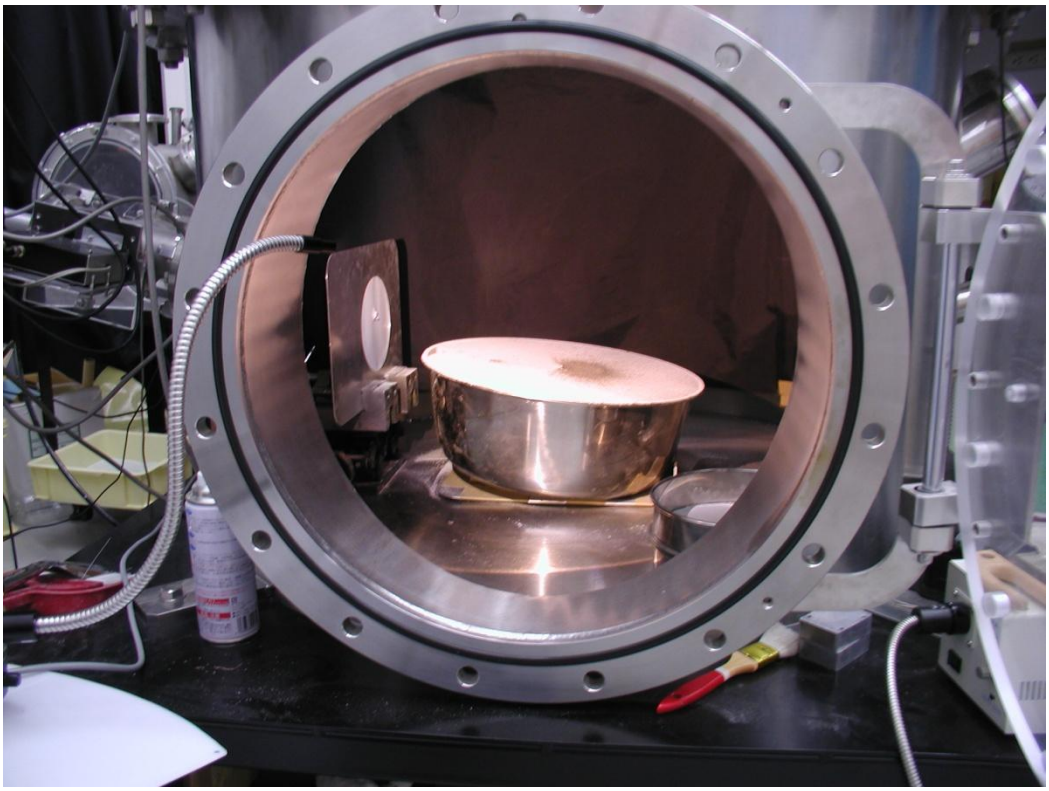

Figure 2.2. Image of the impact chamber set-up at the University of Tokyo laboratory. This image is taken through the main door to the vacuum chamber. The gun is mounted on the 15° gun port (left side of image), and the bowl has been tilted 9° away from the gun, giving a 6° impact angle.

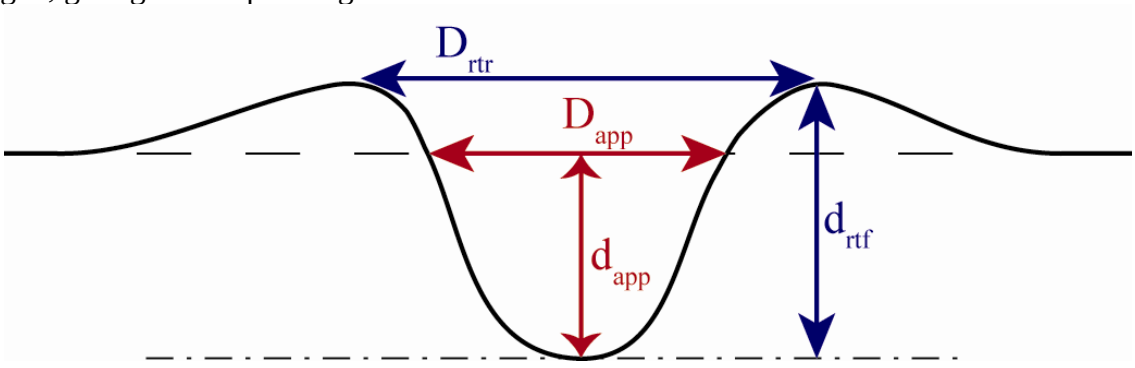

Figure 2.3. Cross-sectional diagram of impact crater showing rim-to-rim and apparent quantities. D_{rtr} is rim-to-rim diameter, d_{rtf} is rim-to-floor depth, D_{app} is apparent diameter, and d_{app} is apparent depth. Dash-dot line represents crater floor. Dashed line represents pre-impact surface.

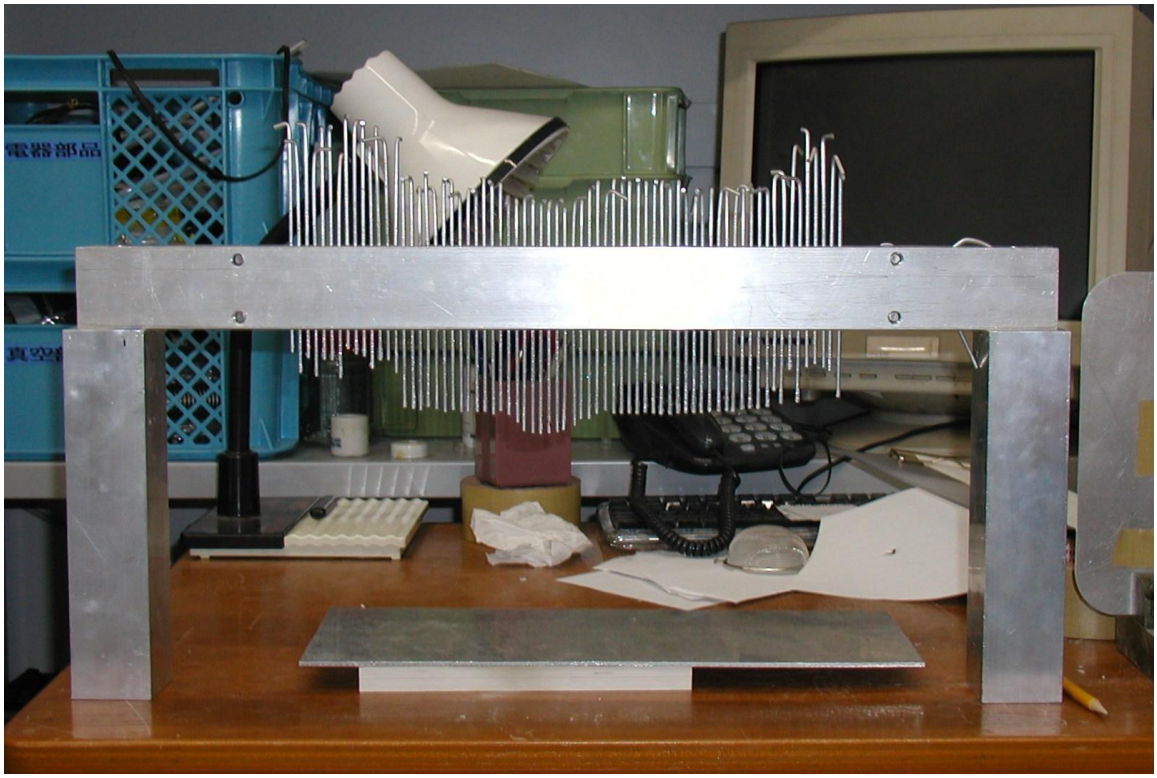

Figure 2.4. Crater Profiler used to take profiles of the experimental craters created at the laboratory at the University of Tokyo. Profiler is positioned over the crater, and metal pegs are lowered to the crater/target surface. The Profiler is then placed on its side and the profile of the metal pegs is traced onto paper.

metal pegs is traced onto paper. These paper profiles were then digitized using a simple program called xyExtract (available free from http://zeus.df.ufcg.edu.br/labfit/index_xyExtract.htm). This program allows one to scan in and load any graph, click on each data point, and then output an ASCII data file of coordinates for each point. This file can easily be imported into Excel (for example) and graphed (Figure 2.5).

Several problems were encountered during the course of the experiments, including malfunction of the laser-velocity recording system, disturbance of the target surface due to blasts of air from the gun, and disturbances of the crater due to the projectile bouncing back into the sand target after creating the crater. These shots were deemed unusable because either the crater and ejecta had been significantly altered or no projectile velocity was recorded. A paper shield was attached to the end of the gun barrel to lessen the amount of air reaching the target and disrupting the flour-dusted surface when the projectile was fired. A black drape was placed inside the chamber to stop the projectile from bouncing around inside the chamber after creating the crater. A total of 50 experimental shots were obtained in the two weeks of work at the lab, of which 34 are deemed useable. Several of the craters were not measured directly for depth, but all of the usable craters were photographed to allow the ejecta distribution to be observed.

Calculating the volume of the crater cavity is an integral part of the analysis of the experimental impact craters and is essential in calculating the mass of material displaced during the impacts. Crater volumes can be estimated using a single direct measurement of crater depth and minimum and maximum crater diameter, and then assuming that the

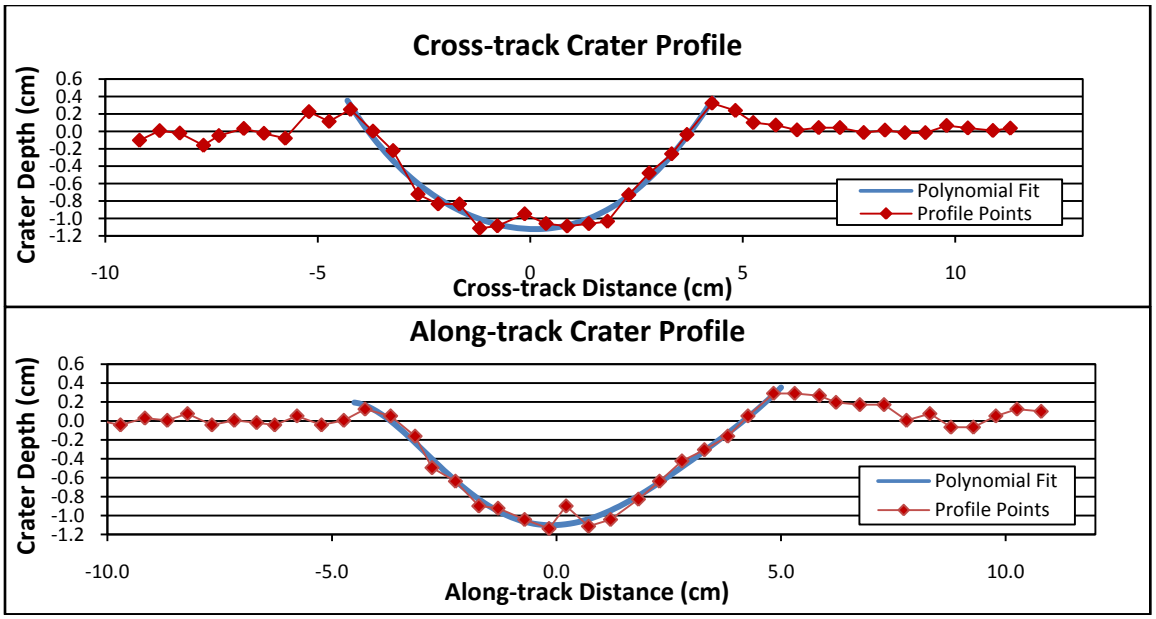

Figure 2.5. Example of a digitized crater profile; cross-track and along track profiles of 25° crater. Profiles points shown here with red diamonds were digitized with xyExtract and plotted in Excel. Blue lines represent the 5th order polynomial best fit line of the crater profile. For reference, y=0 is the approximated pre-impact surface.

craters are elliptical paraboloids (elliptical in plan-view, with parabolic cross sections). The equation for the volume of an elliptical paraboloid is

$$V_{ellip\ parab} = \tfrac{1}{2}\pi r_{min} r_{max} d_{app} \quad (2.1)$$

where d_{app} is the apparent crater depth, and r_{min} and r_{max} are the maximum and minimum apparent radii (all measured relative to pre-existing terrain). However, assuming that the craters have the ideal shape of a perfect elliptical crater rim and parabolic depth profile may be inaccurate.

A second method of computing the volume was developed that reduces the number of assumptions: using the cross-track and along track profiles for each crater that are integrated to determine volume. This method still assumes an elliptical crater rim shape, but uses the crater profile to measure depth (and does not assume a parabolic shape). The digitized profiles are imported into Excel and graphed. Some of the craters have only one profile (in the along track direction). For these 4 craters, the data for the along track profile is also used as the cross-track profile.

Before actual numerical integration can be performed, the height of the original, pre-impact surface has to be determined, the crater profiles must be fit with "best-fit" (via least squares) polynomial functions, and where these profiles intersect the pre-impact surface must be determined. Then for convenience in the integration process, the data is transformed so that the origin of coordinates lies at the center of the crater and on the pre-impact surface.

The height of the pre-impact surface is approximated by averaging the z values (depth) for the points that can be assumed to lie on the relatively flat pre-impact surface

(points on either side of the crater, but not including the crater or rim). Only the portion of the crater wall below the pre-impact surface is considered part of the crater from this point on.

Next, the profiles are imported into MATLAB 7.3.0, and the relevant portion of the crater profile is fit with a polynomial (Figure 2.5). Fifth order polynomials best represented the data, and one or two points on the inside of the rim above the pre-impact surface were also used in these fits, in order to preserve the trend of the profile at the points where it crosses the pre-impact surface. The roots of the polynomial curves are determined so that the center of the fitted crater and its apparent diameter (diameter of the crater at the pre-impact surface) can be found.

The next step involved the subtraction of x and y center values from the data values, effectively moving the coordinates so that the origin is in the center of the crater, and on the pre-impact surface. The curve fitting is then redone for both profiles (in the transformed coordinate system).

The coefficients for the polynomials are recorded, and input into a script that calculates the volume of the fitted crater by dividing the crater into vertical elliptical 'rings' centered about the center of the crater. Each elliptical ring is further broken down into a number of small angular segments (Figure 2.6). The volume of each elliptical ring is found by calculating the surface area of each of the small segments, multiplying that area by the crater depth at each location, and then summing these volumes. Depth at each point is linearly interpolated from the profiles. Adding up the volumes of all these rings gives the volume of the crater.

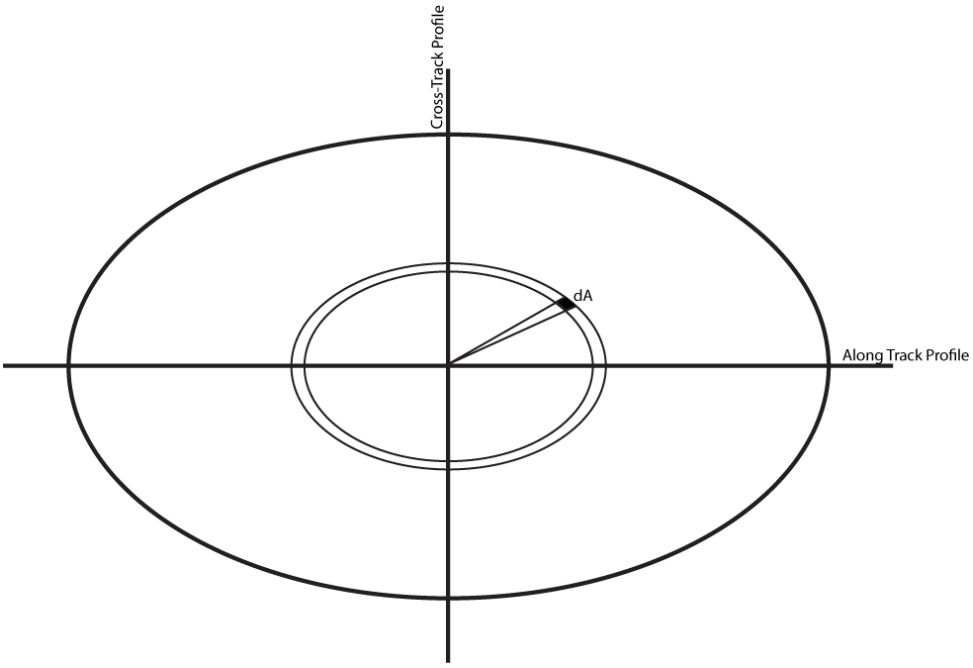

Figure 2.6. Plan-view of crater integration method. The outer ellipse is the crater edge (at pre-impact surface). The two central ellipses represent boundaries of one of the vertical rings used to divide the crater for volume calculation. A shaded area, dA, represents one of the segments used in the integration of the ring. Horizontal and vertical lines represent the location of the along-track and cross-track profiles.

3. Analysis and Results

3.1 Analysis of Experiments

Table 3.1 shows the impact angle, velocity, rim-to-rim diameter, rim-to-floor depth, and apparent depth and diameter for the craters that were deemed useable for this study. Of these 34 craters, only two were not measured directly for depth, and the laser-velocity system malfunctioned only once. Rim-to-rim diameters (in the along track and cross-track directions) were measured directly for all craters. Profiles were taken for 21 of the 34 craters; apparent depth and diameter were calculated for those craters using their polynomial curves and are given in Table 3.1.

3.1.1 Crater Dimensions and Elongation

The maximum diameter was determined for each crater immediately following its formation by using a ruler to measure the maximum rim-to-rim distance in millimeters, along the path the projectile traveled (the along track direction). In most cases, the minimum crater diameter was also measured perpendicular to the path of the projectile (cross-track direction). For the craters for which a profile was acquired, rim-to-rim diameters can also be measured from the profiles. Both sets of maximum rim-to-rim diameters are plotted versus impact angle in Figure 3.1. For nearly all craters, the diameters measured using each technique are within only a few millimeters of each other. Therefore, in this study we have chosen to use the direct measurements rather than

Table 3.1. Experimental Crater Data. Impact angles are measured from horizontal. Rim-to-rim diameters and depths shown here in columns 2, 3, and 4 were measured directly from the craters using a ruler. Apparent (measured with respect to the pre-impact surface) diameters and depths were found by digitizing the profiles and analyzing them as described in section 3.1.2. Maximum rim-to-rim diameters and rim-to-floor depths shown in far right columns were measured from the crater profiles. Craters for which no profiles were taken do not have apparent depth or diameter measurements.

EXPERIMENTAL CRATER DATA									
Impact Angle	Velocity (m/s)	Maximum rim-to-rim Diameter (mm),	Minimum rim-to-rim Diameter (mm)	Rim-to-floor Depth (mm)	Maximum Apparent Diameter (mm)	Minimum Apparent Diameter (mm)	Average Apparent Depth (mm)	Maximum rim-to-rim Diameter (mm)	Rim-to-floor Depth (mm)
		Measured directly from Crater			From Polynomial fit to Profile			From Profiles	
0.5°	167	49	42	3					
1°	162	39	32	3	49.1	49.1	2.711	44	4
1°	176	46	35	3					
2°	154	43	36	4					
2°	171	46	43	3					
3°	152	45	43	Not measured					
3°	149	50	45	6	40.9	34.9	4.139	47	5
4°	152	51	45	6	44.1	38.63	4.0335	49	5
4°	152	55	49	7	44.66	40.32	5.9275	54	7
6°	187	60	56	6	51.06	54.19	3.871	57	5
6°	236	65	60	8	56.36	60	5.4865	66	7
8°	189	60	56	9	55.16	56.27	6.708	65	9
8°	179	61	60	Not measured					
10°	189	62	58	7	57.6	52	5.047	61	7
10°	156	62	61	6					
15°	236	70	70	9	41.94	55.99	6.505	68	8
15°	227	75	75	10	66.95	58.8	7.871	82	8
20°	181	80	75	9	67.62	66.96	7.531	80	9
20°	219	80	80	10	71.46	64.95	7.2475	75	8
25°	Not measured	85	85	12	73.7	72.5	9.3185	87	11
25°	260	90	90	15	74.37	76.27	11.13	94	12
30°	198	95	95	15	82.1	75.4	12.365	98	12
35°	245	105	105	17	97.2	97.2	13.105	106	15
40°	151	90	90	7.5					
40°	192	93	93	8	85.94	85.94	8.667	96	10
45°	144	95	95	8	85.65	73.31	7.83	96	9
45°	162	98	98	9	89.99	75.63	9.775	99	11
45°	205	100	100	9					
50°	216	98	98	9					
60°	176	99	99	10					
65°	174	100	100	12	83.27	83.27	12.46	103	16
75°	162	105	105	11					
90°	179	105	105	11					
90°	181	107	107	11	82.84	82.84	10.64	101	13

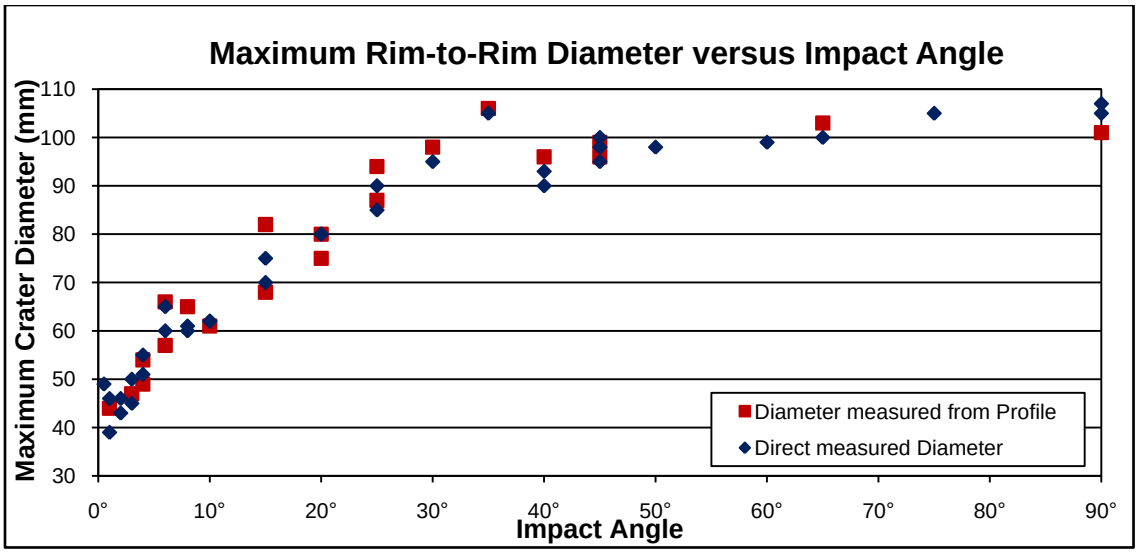

Figure 3.1. Maximum rim-to-rim diameter versus impact angle for low velocity experiments. Blue triangles represent diameters that were measured directly from the impact craters. Red squares represent diameters measured from crater profiles. Note the change in trend occurring at impact angles of 35°-40°.

measurements from a profile whenever possible in order to include those craters for which a profile was not taken. Figure 3.2 shows the maximum diameter (measured directly from the craters) versus impact angle with two separate trend lines, one for impact angles 0.5°-35°, and one for 40°-90°. Diameter generally increases with increasing impact angle. However, craters with impact angles of 35° and below exhibit one trend while those above 35° have a differing, shallower trend. Craters in the 0.5°-35° impact angle group show an average diameter increase of 1 to 2 mm for every degree increase in impact angle, as indicated by the slope of the best fit line (1.74 mm/degree). The slope of the best fit line for the 40°-90° impact angle group indicates a much smaller diameter change of only 0.25 mm/degree.

Examining crater depth versus impact angle also shows a significant change in trend and value at about 35° (Figure 3.3). The crater with an impact angle of 35° (17 mm depth) is more than twice as deep as both craters at 40° (7.5 mm and 8 mm). Crater wall slumping was initially thought to be a possibility for this noticeable change at 35°. When wall slumping occurs, the crater wall fails and collapses into the crater, increasing the diameter and shallowing the depth. However, the opposite relationship is seen in these experiments. Onset of wall slumping at a particular impact angle is therefore not thought to be the cause for the noted change in diameter and depth at 35°.

Elongation is defined here as the ratio of the along track crater diameter to the cross-track diameter (maximum diameter/minimum diameter for most craters), and is a useful tool in describing the shape of the crater rim. Elongation is plotted versus impact angle in Figure 3.4, using both the rim-to-rim diameter measurements and the

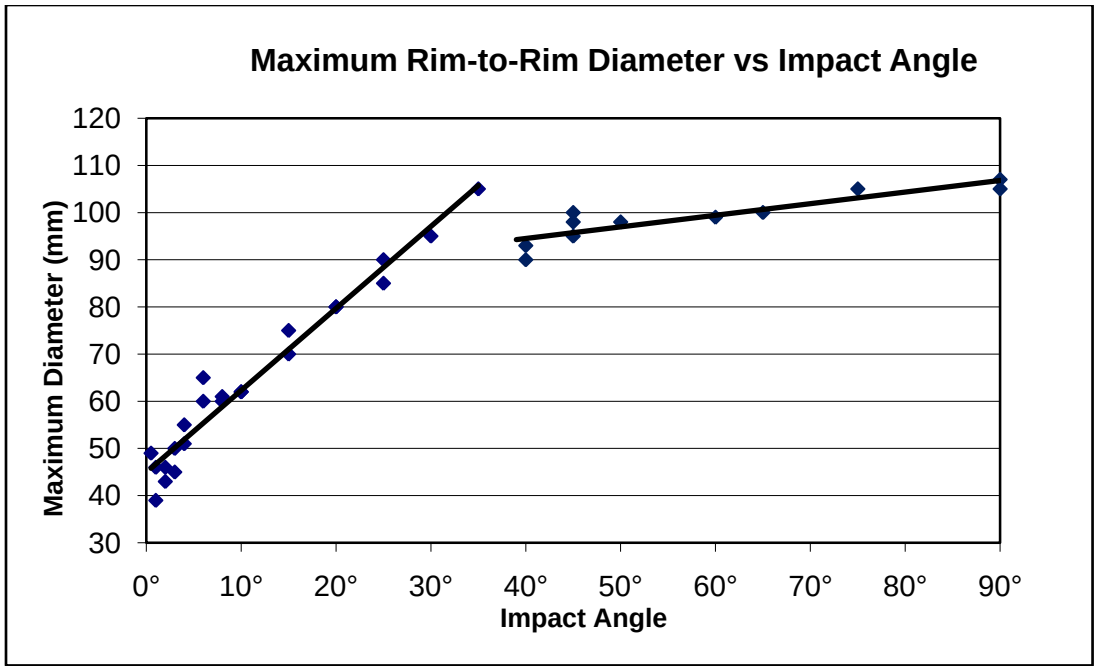

Figure 3.2. Maximum rim-to-rim diameter versus impact angle, showing trend lines. Diameters shown were measured directly from the craters. Trend lines shown are best fit lines for the two groups of data points. The slope for the 0.5°-35° impact angle group best fit line is 1.74, and the slope for the 40°-90° impact angle group best fit line is 0.25.

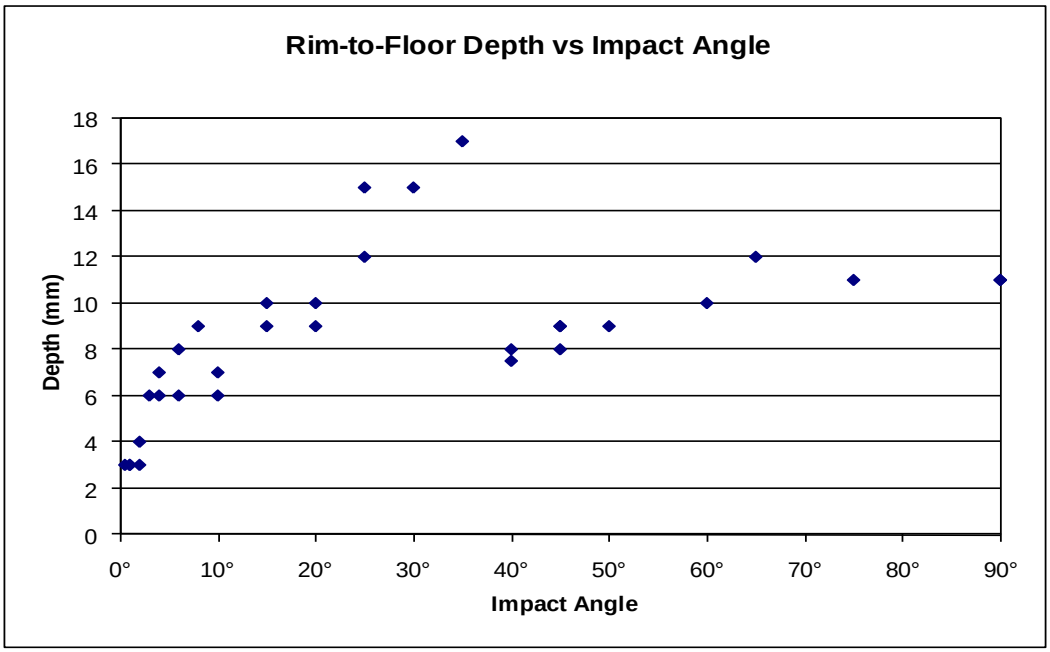

Figure 3.3. Rim-to-floor depth versus impact angle. Depths and diameters were measured directly from the craters. Note the change in trend occurring at impact angles of 35°-40°.

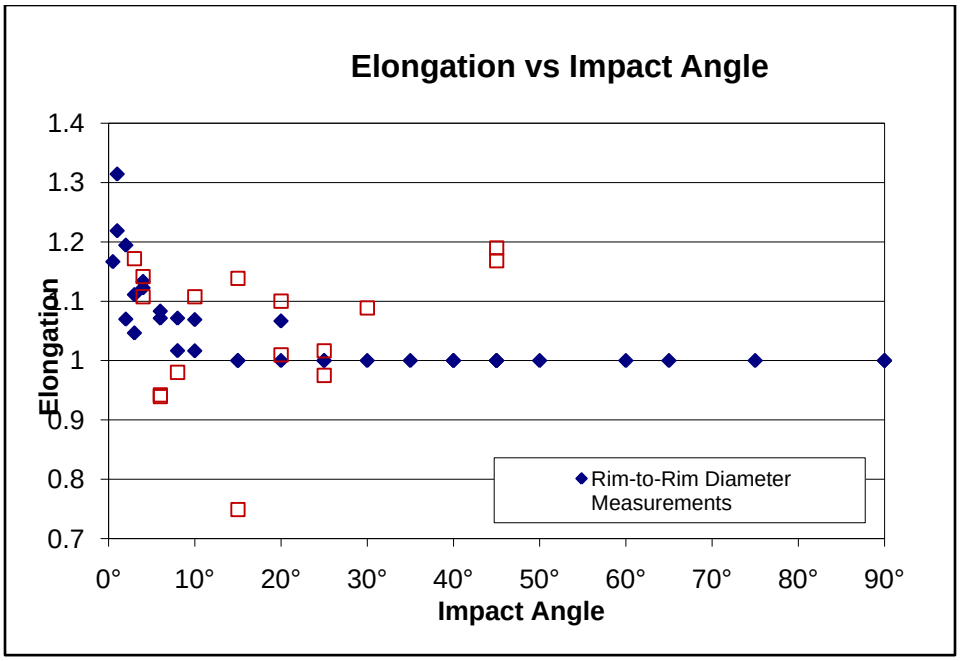

Figure 3.4. Elongation versus impact angle. Elongation is defined here as the ratio of the along track diameter to the cross-track diameter. Solid blue diamonds represent elongations calculated using the rim-to-rim diameter measured directly from the crater. Red open squares represent elongations calculated using the apparent diameters that were found after digitizing the crater profiles.

apparent diameter measurements. It should be noted that no craters were actually elongate in the cross-track direction; elongations less than 1 in the apparent diameter dataset are due to small inaccuracies in the process of using the profiles to pick the apparent diameter, mainly in defining the pre-impact surface. Craters remain circular (elongation of ~1) down to impact angles of ~15° from horizontal. Below 15°, craters become increasingly more elliptical as impact angle decreases. It should be noted that no apparent change in the trend of the elongation is seen at or near impact angles of 35°, as is apparent with the data for depth and diameter.

3.1.2 Crater Volume

Profiles were acquired for 21 craters in the experimental dataset. Both of the volume estimates for all craters are plotted versus impact angle in Figure 3.22. For most craters, the two volumes are nearly the same. This would suggest that the craters *are* roughly shaped like elliptical paraboloids, and the elliptical paraboloid approximation is a reasonable one. This information is useful to others doing crater experiments because the process of collecting the profiles is very tedious and time consuming. The process of calculating volume is also magnitudes faster when using the elliptical paraboloid assumption (minutes for the entire dataset versus hours per crater when using the profiles).

Craters with impact angles below 35° exhibit a fairly constant trend in volume displaced, with volume increasing with impact angle (Figure 3.6). However, craters

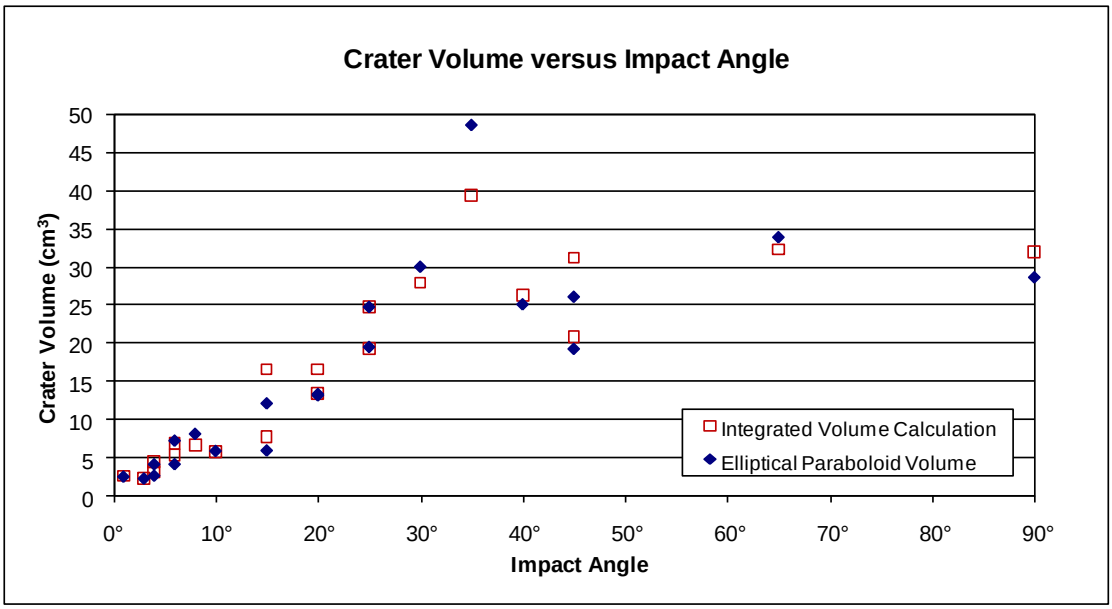

Figure 3.5. Crater volume versus impact angle. Solid blue diamonds represent volumes calculated using the integration method. Red open squares represent volumes calculated using the simplified geometry of an elliptical paraboloid (apparent depth and apparent diameter were found using profiles). The two volumes for each crater are nearly the same, suggesting that the craters are elliptical paraboloids.

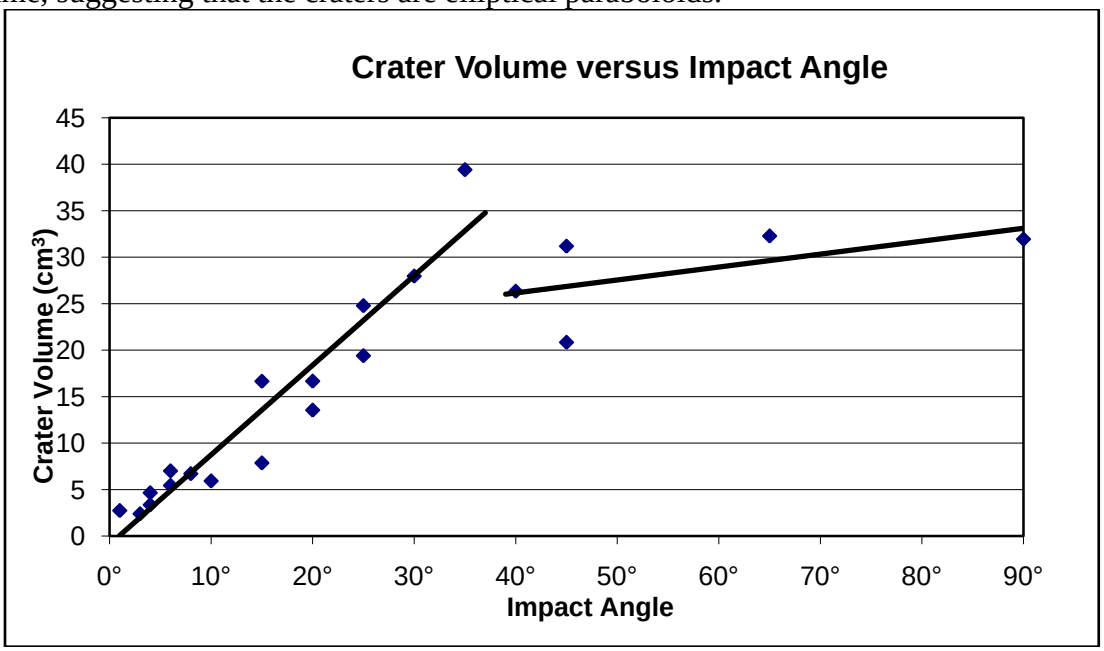

Figure 3.6. Crater volume versus impact angle, highlighting change in trend at 35°. All volumes plotted here were generated using the integration method. The data is divided into two subgroups, craters with impact angles of 35° or less, and craters with impact angles greater than 35°. The two subgroups are each fitted with a best-fit line to emphasize the change in trend at 35°.

above 35° seem to follow a shallower trend that is offset to lower values, much like was seen with the diameter versus impact angle data.

Crater volume is used to calculate the mass of material displaced from the crater (M_{crater}, from equation (1.2) above) by multiplying it by the density of the target material (Figure 3.7). Mass displaced is a quantity commonly used to compare sets of impact experiments, generally by calculating cratering efficiency (π_v, equation 1.2) or mass ratio (equation 1.3).

3.1.3 Depth to Diameter Ratio

Depth to diameter ratio is a quantity commonly used in statistical studies of planetary crater populations designed to explore surface properties and processes. As such, characterization of how it varies with impact angle may be useful. Figure 3.8 shows depth to diameter ratio versus impact angle for the experimental craters. Two sets of depth/diameter ratios are shown here. Closed diamond points are computed using the rim-to-rim diameter and floor-to-rim depths. Open square points use apparent diameter and apparent depth (those attained using the profiles for each crater, measured with respect to the pre-impact surface). An average is used in cases where more than one diameter is known (this includes elongate craters and most of the apparent diameter points). There is a large amount of scatter in the data, but it is still clear that there is a change in the trend of the data at an impact angle of 35°.

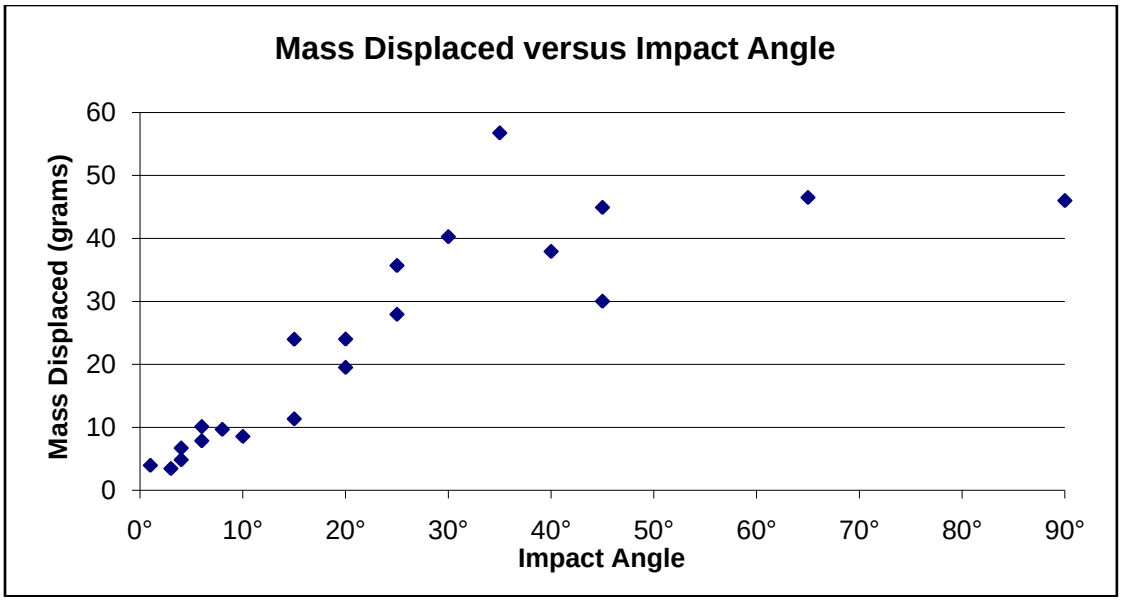

Figure 3.7. Mass of material displaced by impact versus impact angle for low velocity lab experiments. Mass is calculated by multiplying the density of the target material with the volume of the crater (computed using integration method).

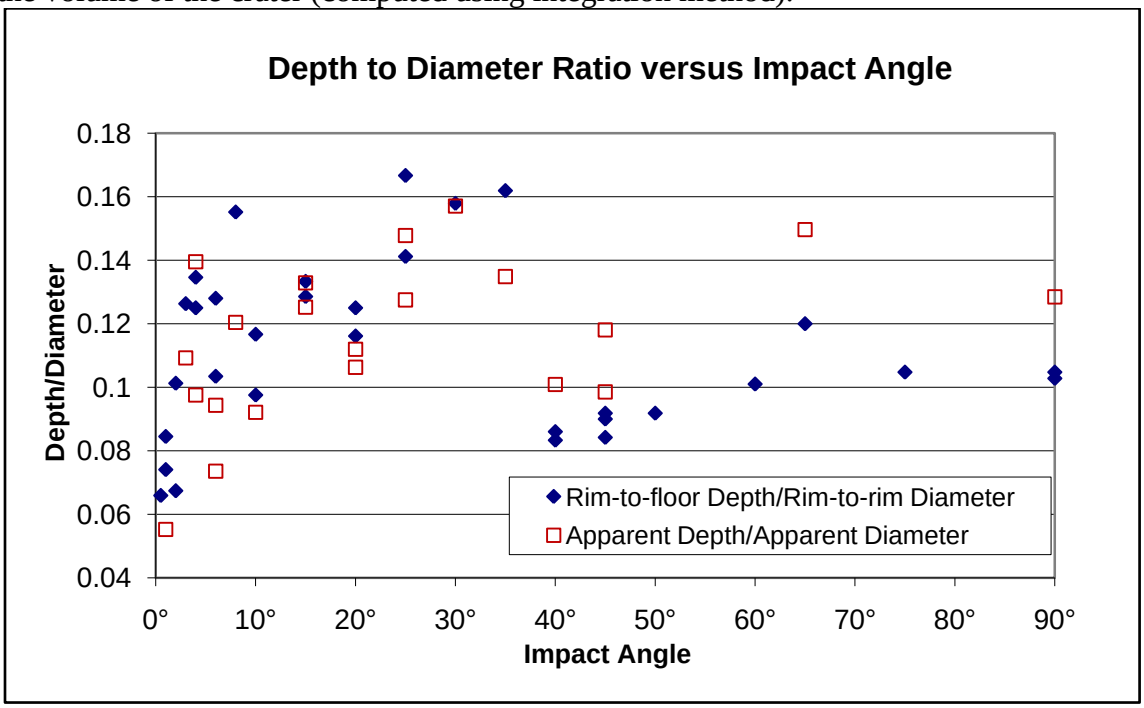

Figure 3.8. Depth to diameter ratio versus impact angle. Closed diamond points are computed using the rim-to-rim diameter and floor-to-rim depths (quantities measured directly from the crater using a ruler). Open square points use apparent diameter and apparent depth (those attained using the polynomial fits to the profiles for each crater, measured with respect to the pre-impact surface).

3.1.4 Crater Wall Slope

Slopes of interior crater walls are useful for analyzing how crater shape changes with impact angle. In particular, I looked at how the uprange wall slope compares to the downrange wall slope for each crater. Figures 3.9 and 3.10 show the digitized profiles for each crater. Wall slopes were acquired by importing the along-trajectory profile into MATLAB (as was done for the volume calculations). In calculating slope, the crater wall is the portion of the crater starting at the crater rim (highest point) and extending downward until there is a break in slope (crater floor). Best fit lines were then fit to the portion of the profile that represents the uprange and downrange wall. The slope for each of these best fit lines is the number I used for the wall slope. Wall slopes are plotted versus impact angle in Figure 3.11 and 3.12. Blue diamonds represent slopes for the uprange wall of each crater. Open squares represent downrange wall slopes. The crater at 90° (vertical), by definition, does not have an uprange or downrange wall. However, slopes of two opposing walls for that crater were calculated, and are plotted in the graph (blue triangles). In Figure 3.12, yellow bars indicate craters for which the uprange wall is steeper than the downrange wall and light blue bars indicate craters for which the downrange wall is steeper. Note craters at 4° and 6°. Two craters exist at each impact angle: in both cases one crater has a steeper uprange wall and one has a steeper downrange wall. All craters above 10° have an uprange wall that is steeper than the downrange wall. Craters below 10° have downrange walls that are steeper than the uprange walls, except craters at 4° and 6° (as noted above).

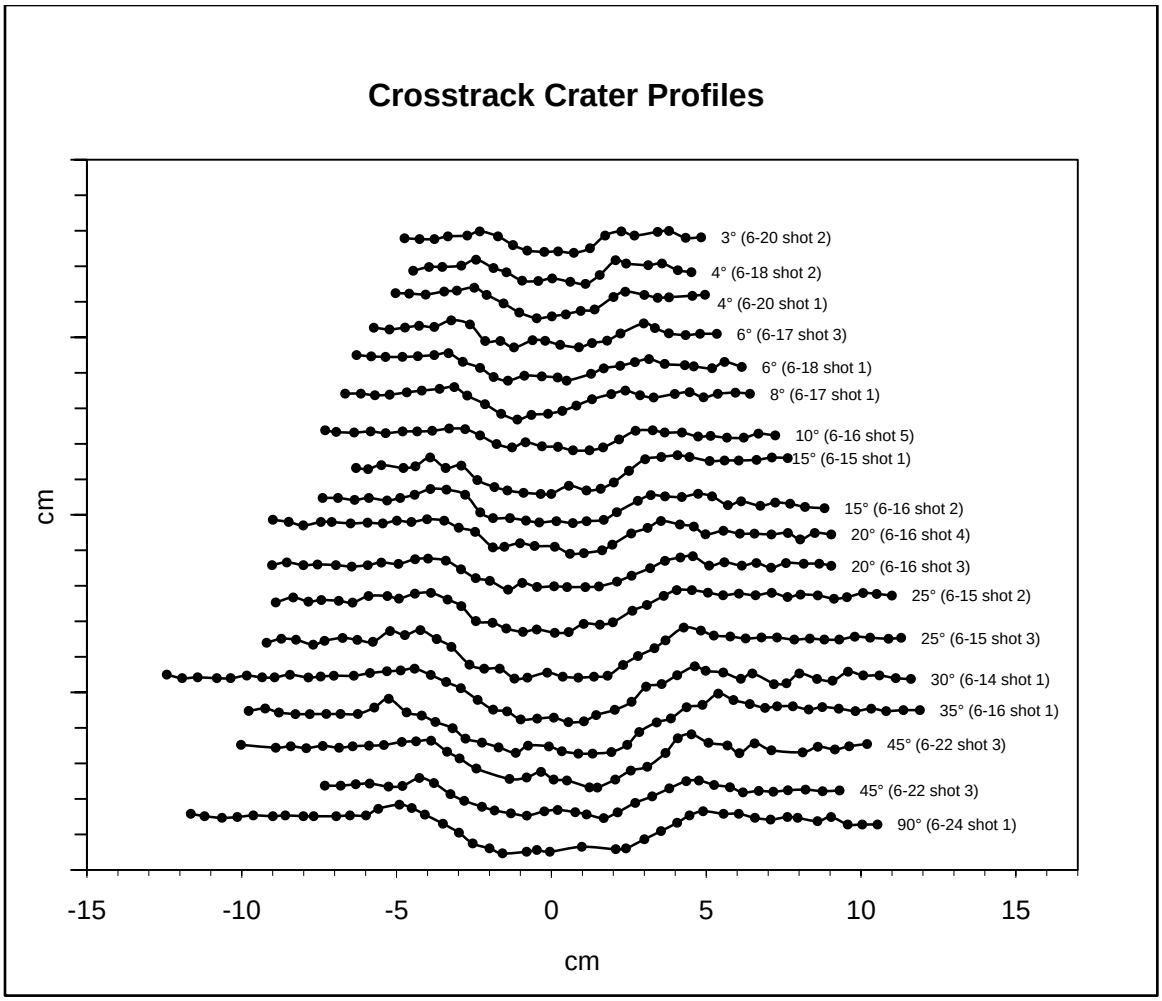

Figure 3.9. Crosstrack crater profiles. Vertical and horizontal axes are in centimeters, with no vertical exaggeration. Each profile is labeled with date and shot number, as well as the impact angle of the projectile.

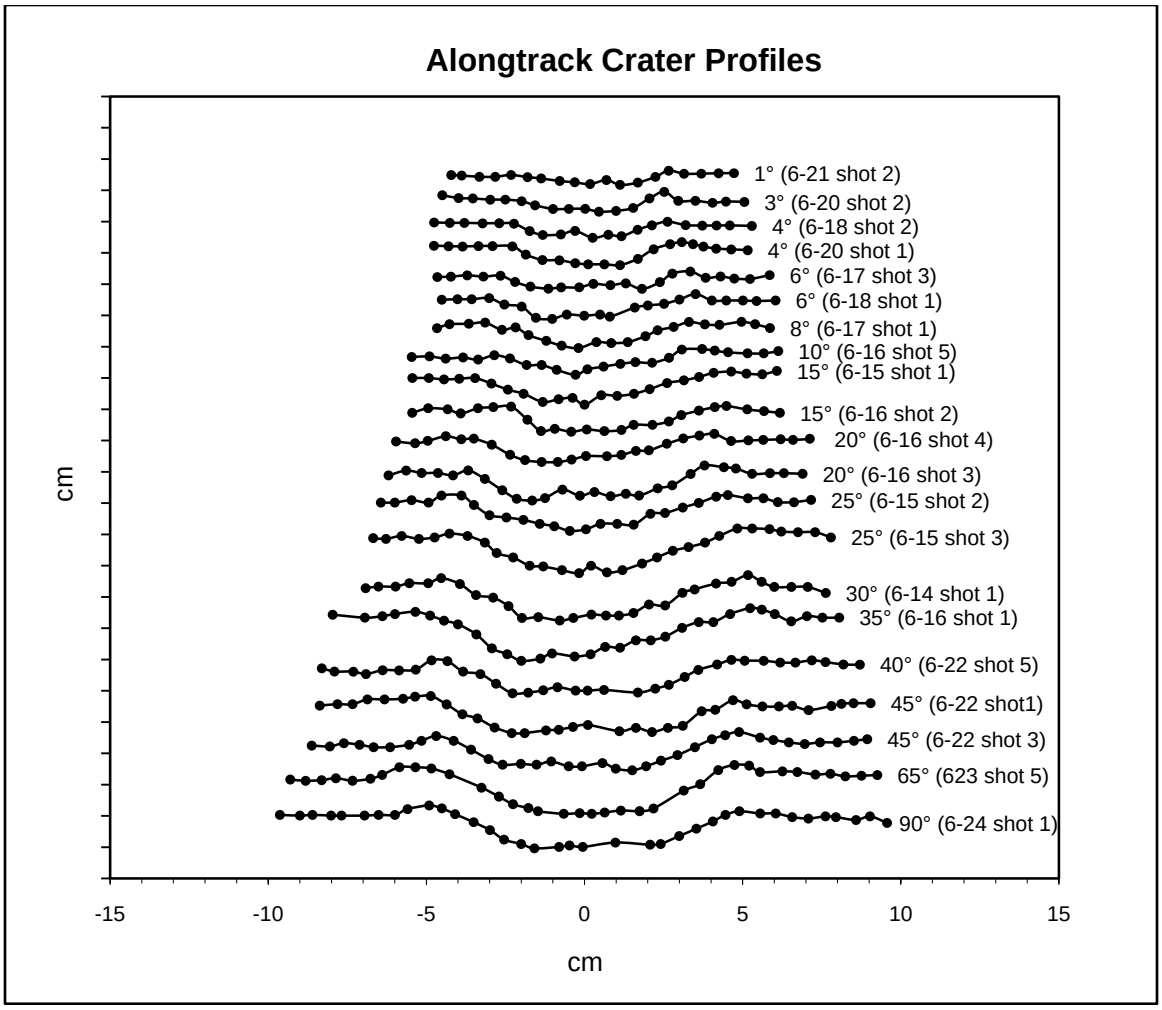

Figure 3.10. Alongtrack crater profiles. Vertical and horizontal axes are in centimeters, with no vertical exaggeration. Each profile is labeled with date and shot number, as well as the impact angle of the projectile.

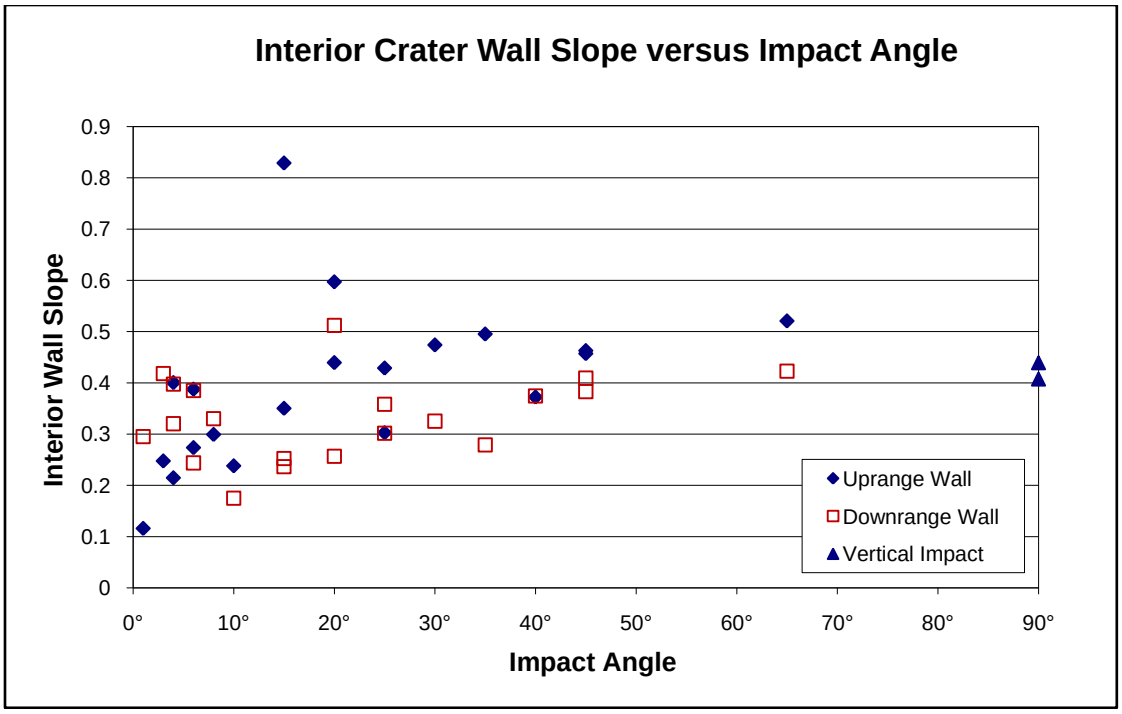

Figure 3.11. Interior Crater Wall Slope versus Impact Angle for low velocity impact experiments. Blue diamonds represent slopes for the uprange wall of each crater, red open squares represent the downrange walls. The crater at 90° (vertical), by definition, does not have an uprange or downrange wall. However, slopes of two opposing walls for that crater were calculated, and are plotted in the graph (blue triangles).

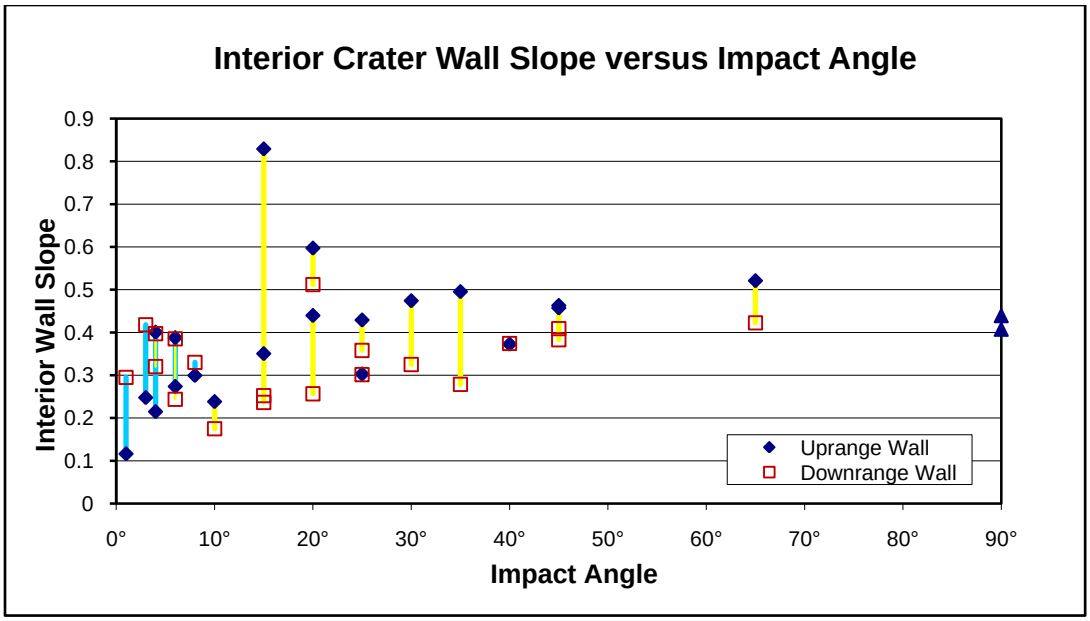

Figure 3.12. Interior Wall Slope versus impact angle, illustrating trend in wall steepness with impact angle. Blue diamonds represent slopes for the uprange wall of each crater, red open squares represent the downrange walls. The crater at 90° (vertical), by definition, does not have an uprange or downrange wall. However, slopes of two opposing walls for that crater were calculated, and are plotted in the graph (blue triangles).Yellow bars indicate craters for which the uprange wall is steeper than the downrange wall. Light blue bars indicate craters for which the downrange wall is steeper. Note craters at 4° and 6°. Two craters exist at each impact angle: in both cases one crater has a steeper uprange wall and one has a steeper downrange wall. All craters above 10° have an uprange wall that is steeper than the downrange wall. Craters below 10° have downrange walls that are steeper than the uprange wall, except craters at 4° and 6° (as noted above).

3.1.5 Ejecta Distribution

The ejecta planform for each crater (See the appendix for images of each crater) was examined in order to gain a clear picture of the progression of how the ejecta distribution changes with impact angle. This was done by examining the images of the final craters and identifying the presence or absence of ejecta material in the uprange and downrange directions for the various impact angles. Ejecta is symmetric about the crater from vertical (90°, Figure 3.13) to approximately 60°. The ejecta begins to be asymmetric at impact angles of approximately 60° from horizontal (Figure 3.14), and a clear uprange forbidden zone develops around 20° (Figure 3.15). As impact angle decreases below 20°, the uprange forbidden zone continues to increase in size, and less ejecta is located in the downrange direction (Figures 3.16, 3.17, and 3.18). At impact angles around 6° and lower, there is still a clear uprange forbidden zone and very little ejecta is present in the downrange direction, so that most of the ejecta is concentrated in the cross-track direction. It is important to note that there is always some ejecta present in the downrange direction, even at the lowest impact angles; a 'butterfly' ejecta pattern was never seen (Figure 3.18).

3.1.6 Change in Data Trend at 35°

A change in data trend at impact angles of 35° is noticeable in the diameter, depth, volume, and depth to diameter ratio data. Examining the timeline for when experiments at each impact angle were conducted (Figure 3.19) shows that all craters

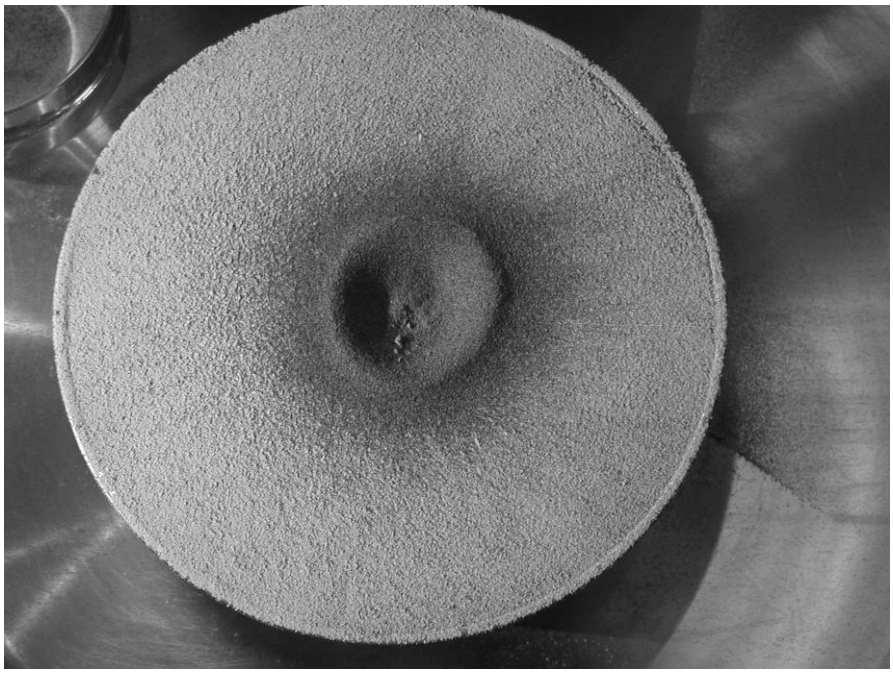

Figure 3.13. Image of 90° impact. Crater is 107 mm across. Ejecta is symmetric about the crater.

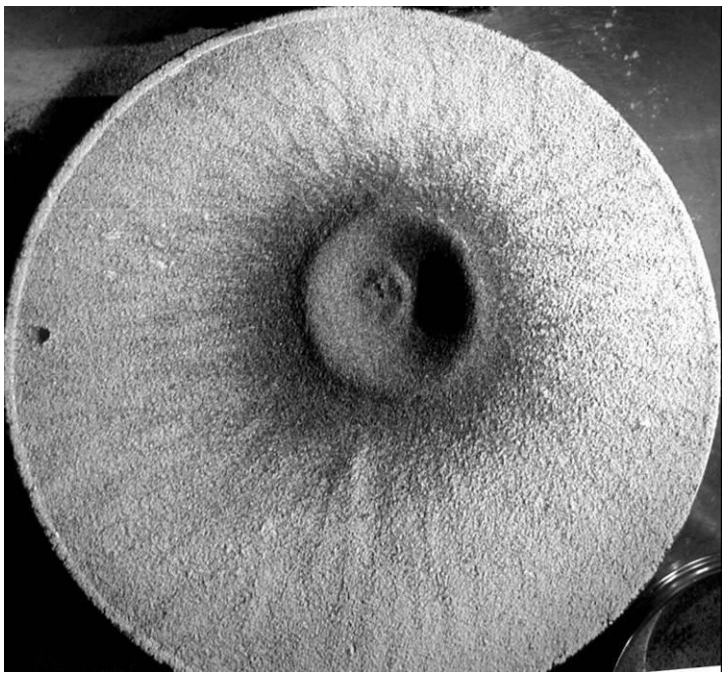

Figure 3.14. Image of 60° impact. Crater is 99 mm across. Ejecta is beginning to be offset in the downrange direction. Projectile trajectory is from top to bottom.

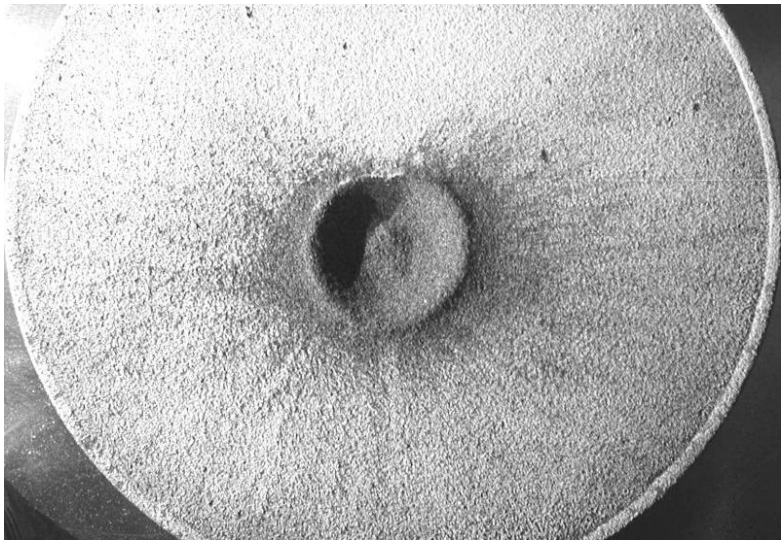

Figure 3.15. Image of 20° impact. Crater is 80 mm across. An uprange forbidden zone is beginning to form. Projectile trajectory is from top to bottom.

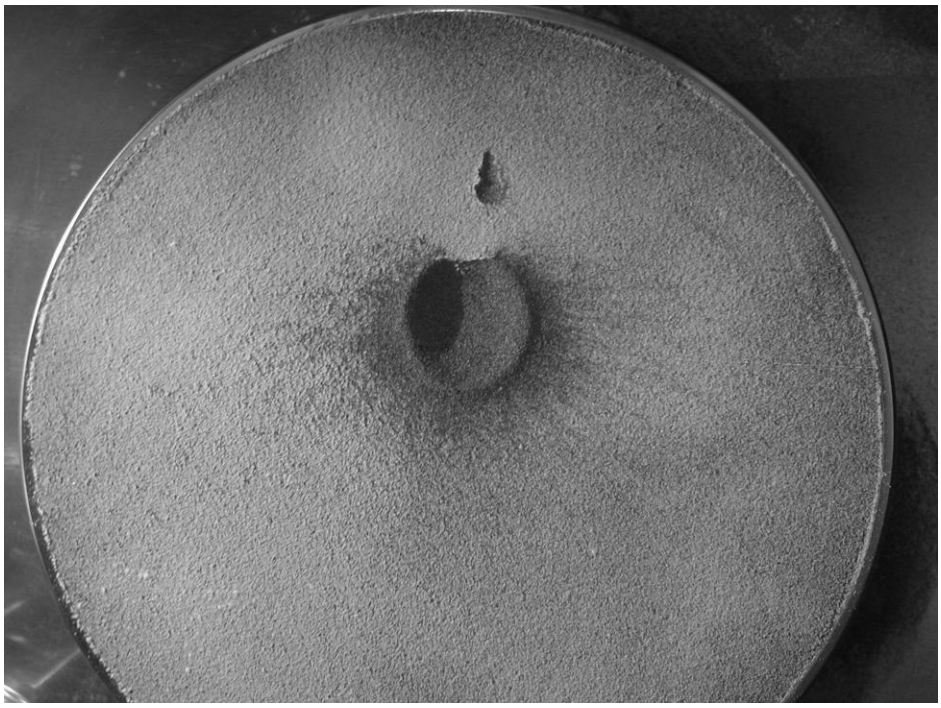

Figure 3.16. Image of 8° impact. Crater is 60 mm x 56 mm. There is a very clear uprange forbidden zone. Projectile trajectory is from top to bottom. (Small pit above crater is from rogue piece of paper.)

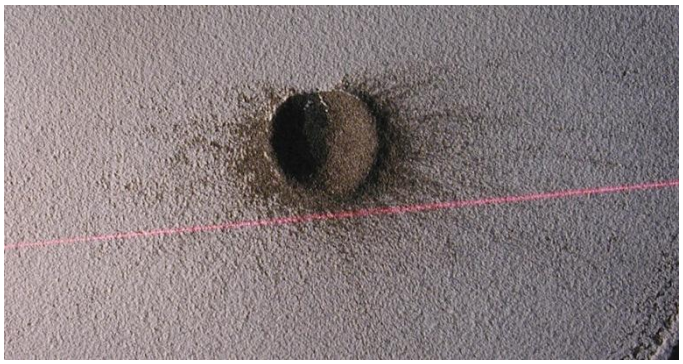

Figure 3.17. Image of 4° impact. Crater is 55 mm x 49 mm. Ejecta is concentrated in the crossrange direction. Projectile trajectory is from top to bottom.

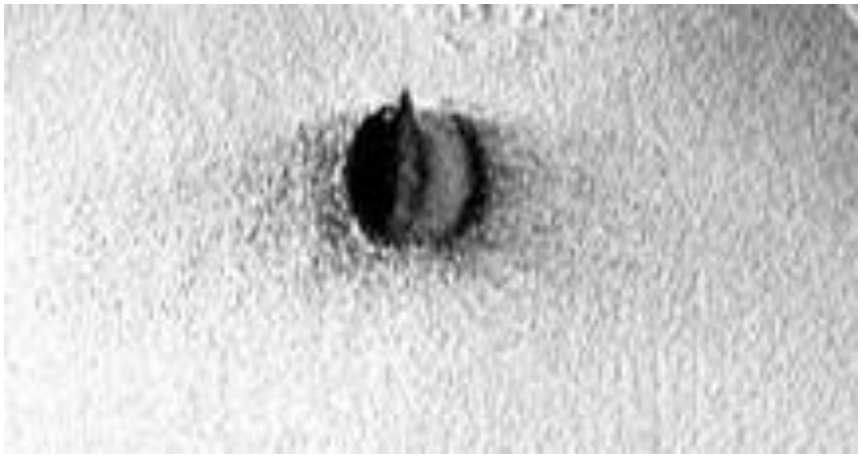

Figure 3.18. Image of 0.5° impact. . Crater is 49 mm x 42 mm. Ejecta is concentrated in the crossrange direction, with some ejecta still present in the downrange direction. Projectile trajectory is from top to bottom.

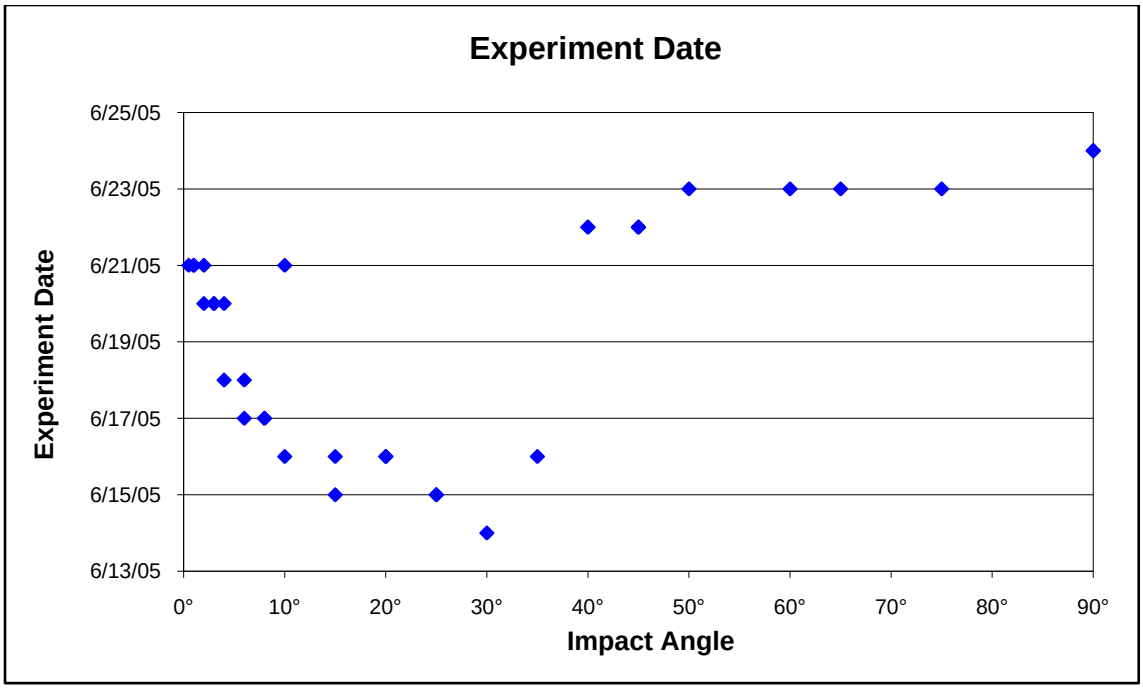

Figure 3.19. Experiment date versus impact angle. Note that all experiments with impact angles of 40° and above were conducted in the last three days of work at the lab.

with impact angles of 40° and higher were conducted in the last three days of work at the lab. It is therefore possible, however unlikely, that some systematic change in experimental procedure took place that caused the observed changes. Such a cause for these noticeable changes in data is highly unlikely, since no memorable change in equipment, methods, or personnel took place at all during the course of the experiments.

The higher angle impacts having slower velocities could account for the craters being generally smaller at higher angles (smaller diameters and shallower depths). Projectile velocity versus impact angle is shown in Figure 3.20. Velocity and crater size data are also given in Table 3.1. To see if differences in velocity could account for this change at 35°, a simple scaling based on energy can be applied.

To do this simple scaling based on energy, start by equating the portion of the kinetic energy of the projectile that goes into excavation of the crater to the potential energy change due to moving the ejecta material from its pre-impact location to its post-impact location. Equating kinetic energy to potential energy gives

$$\tfrac{1}{2}\, m v^2 \bullet f = \rho V g\, \Delta h\,, \tag{3.1}$$

where m is the mass of the projectile, v is the velocity of the projectile, f is the fraction of the total kinetic energy that goes into excavation, ρ is the density of the target material, V is the volume of the resultant crater, g is acceleration due to gravity, and Δh is the change in height of the ejecta material. Rearranging the above equation to solve for the volume of the crater gives

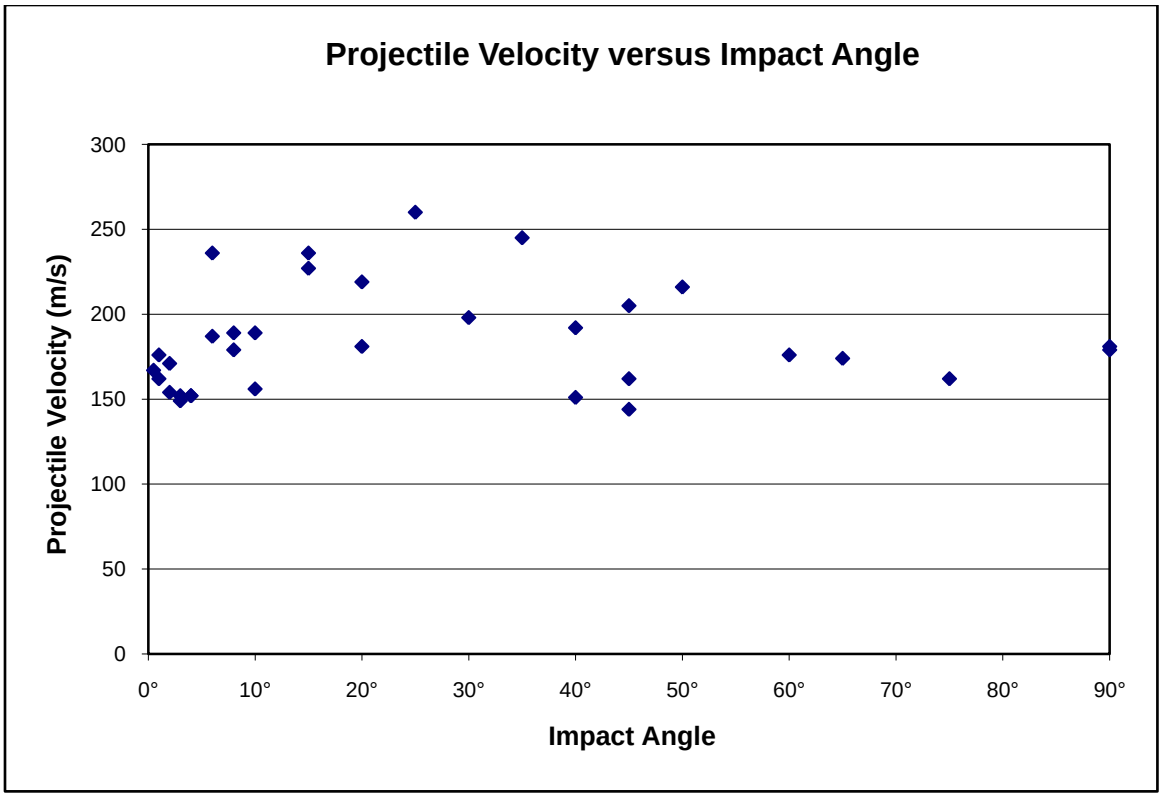

Figure 3.20. Projectile velocity versus impact angle.

$$V = \left(\frac{mf}{2\rho g \Delta h} \right) v^2. \tag{3.2}$$

Quantities can then be inserted into equation 3.2, resulting in one equation for the actual crater and one equation that represents the adjusted velocity crater:

$$V_{actual} = \left(\frac{mf}{2\rho g \Delta h} \right) v_{actual}^2 \tag{3.3}$$

$$V_{adjusted} = \left(\frac{mf}{2\rho g \Delta h} \right) v_{adjusted}^2 \tag{3.4}$$

All of the crater volumes can now be scaled to the same impactor velocity of 200 m/s by dividing equation 3.3 by equation 3.4. Cancelation of like terms gives

$$V_{adjusted} = \left(\frac{v_{adjusted}^2}{v_{actual}^2} \right) V_{actual.} \tag{3.5}$$

200 m/s was chosen as the velocity that all craters would be scaled to for this study ($v_{adjusted}$). For each crater in the experimental dataset, all quantities on the right hand side of equation 3.5 are known. Only a simple calculation is then necessary to scale each crater to the same impact velocity. The velocity adjusted crater volumes and the non-adjusted volumes are plotted versus impact angle in Figure 3.21. This simple velocity scaling does a reasonable job of accounting for the change in data value and trend visible at impact angles of 35°. We assume then, that this change at 35° is likely due to differences in impactor velocity, and is not related to impact angle.

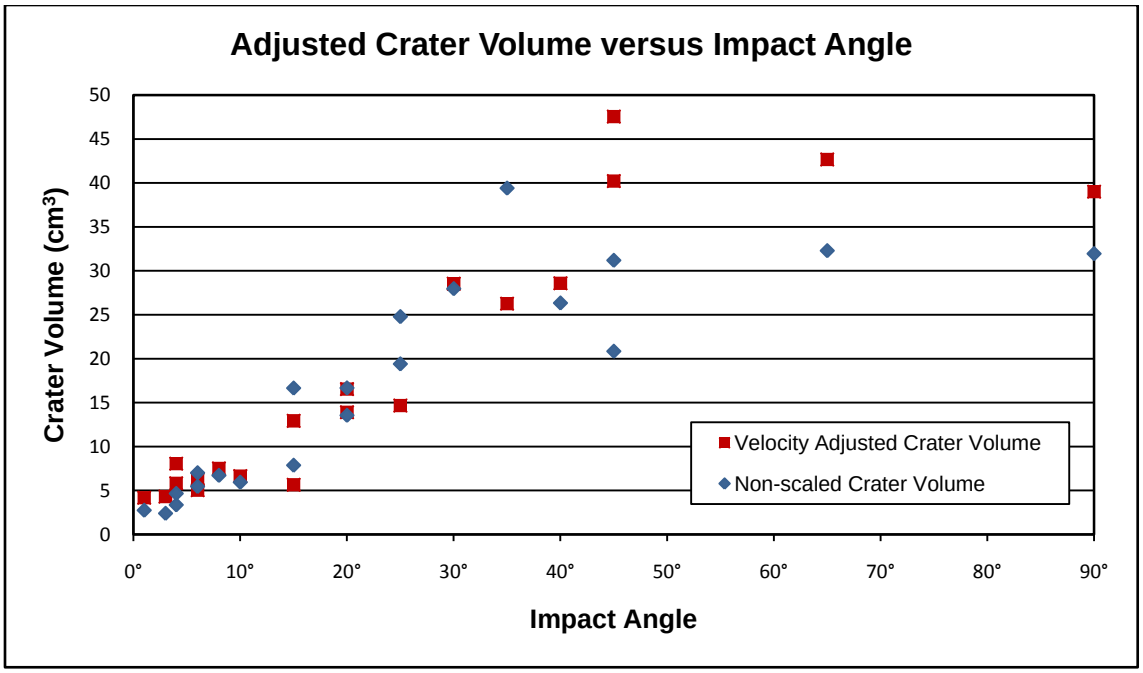

Figure 3.21. Velocity adjusted crater volume versus impact angle. Red squares are crater volumes that have been scaled to impact velocities of 200 m/s using equation 3.5. Blue diamonds are non-velocity scaled crater volumes calculated using the integration method.

3.2 Comparison to Gault and Wedekind (1978)

When comparing the published data of Gault and Wedekind (1978) to my own experimental data, it is important to note that most of their data is plotted using data points that represent an unknown number of actual experimental craters. Gault and Wedekind did not publish the actual numbers for depth, diameter, or volume of their craters, only allowing for comparisons of (normalized) displaced mass, elongation, wall slope, and depth to diameter ratio. It is also important to note that the Gault and Wedekind experiments have much larger impact angle increments (craters were created only every 15° between vertical and 30°), compared to every 5° or 10° with the low-velocity experiments.

Gault and Wedekind show data for impacts into several different target materials (quartz sand, pumice dust, and granite) and two different projectile types (aluminum and pyrex). Since their experiments into quartz sand using pyrex projectiles most closely match my laboratory materials, those are the results that are used in the comparison, unless stated otherwise.

The published elongation and depth to diameter ratios of Gault and Wedekind are given in terms of apparent diameters and depths (measured with respect to the pre-impact surface). It would be useful to be able to compare these ‘apparent’ ratios to those ratios calculated using the direct measured rim-to-rim and rim-to-floor diameter and depth from the experiments I conducted at lower velocities at the laboratory in Japan.

Start by revisiting the assumption that vertical cross-sections of the craters are approximately parabolas, where x is in the along-track direction, y is in the cross-track direction, and z is the depth. The equations for these parabolas are

$$\text{Along-track:} \quad x^2 = (4p_a)z \tag{3.1}$$

$$\text{Cross-track:} \quad y^2 = (4p_c)z \tag{3.2}$$

where p_a and p_c are constants and the vertices of the parabolas lie at the origin. Thus, the bottom of the crater lies at the origin for mathematical convenience. When z equals the apparent depth, x is one half the maximum apparent diameter and y is one half the minimum apparent diameter. When z equals the rim-to-floor depth, x is one half the maximum rim-to-rim diameter and y is one half the minimum rim-to-rim diameter. Therefore, using equations 3.1 and 3.2:

$$\text{Elongation} = \frac{D_{max}}{D_{min}} = \frac{2x}{2y} = \frac{2\sqrt{4p_a z}}{2\sqrt{4p_c z}} = \sqrt{\frac{p_a}{p_c}} = \text{Constant.} \tag{3.3}$$

The above equation shows that elongation is a ratio of the parameters (constants) for the parabolas, and does not depend upon the height at which diameters are measured. Elongation should be the same regardless of whether both diameters are measured at the pre-impact surface or at the crater rim. The rim-to-rim measured elongations of my experiments are thus directly comparable to the apparent diameter elongations of Gault and Wedekind.

Similarly, the depth to diameter ratio can be examined by first rearranging equation 3.1 to solve for depth:

$$\text{Depth} = z = \frac{x^2}{4p_a}. \tag{3.4}$$

Recalling that diameter equals 2x, we can evaluate the depth to diameter ratio as follows:

$$\frac{\text{Depth}}{\text{Diameter}} = \frac{z}{2x} = \frac{x}{8p_a} = NOT\text{Constant}. \tag{3.5}$$

The above equation shows that the depth to diameter ratio is not constant; the ratio is dependent on whether apparent or rim-to-rim measurements are used. My rim-to-rim and rim-to-floor measurements are therefore not comparable to the apparent depth and diameter measurements of Gault and Wedekind.

3.2.1 Crater Elongation

As in section 3.1.1, elongation is defined as the ratio of the along track crater diameter to the cross track crater diameter (maximum diameter/minimum diameter). Gault and Wedekind's published elongation data is given in terms of apparent diameters, while the elongations for my experiments were calculated using the measured rim-to-rim diameters. As explained above and shown in equation 3.3, these sets of elongation data are directly comparable. Figure 3.5 shows elongation versus impact angle for both sets of experiments. Yellow triangles represent elongations calculated using the rim-to-rim diameter measured directly from the crater. Blue diamonds represent points from Gault and Wedekind's impacts. Gault and Wedekind's eight data points represent 121 rounds fired into quartz sand with velocities of 3.6-7.2 km/sec. Error bars are standard deviations, as shown in Gault and Wedekind's figure (error bars are smaller than the data

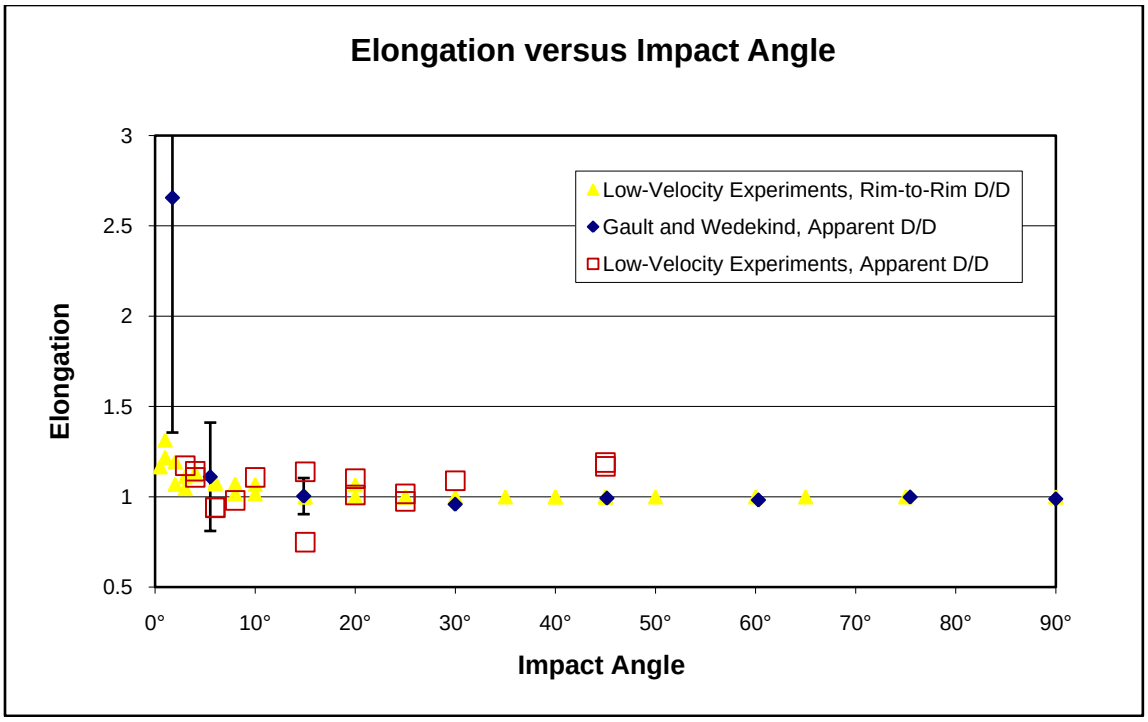

Figure 3.5. Elongation versus Impact Angle. Elongation is defined here as the ratio of the along track diameter to the cross-track diameter. Yellow triangles represent elongations calculated using the rim-to-rim diameter measured directly from the crater. Red squares represent elongations calculated using the apparent diameters that were found after digitzing the crater profiles. Blue diamonds represent points from Gault and Wedekind's impacts. These eight data points represent 121 rounds fired into quartz sand with velocities of 3.6-7.2 km/sec. Error bars are standard deviations (error bars are smaller than the data point symbol for their higher angle data points).

point symbol for their higher angle data points). The elongation data for my experiments align well with the elongations from Gault and Wedekind, except at very low impact angles. At angles less than ~5°, Gault and Wedekind's data, of which there is only one point at ~2°, has an elongation that is more than twice as high as the average elongation for my data with similar impact angles. This suggests that lower velocity experiments may not be comparable to high velocity experiments for the near-grazing impacts.

3.2.2 Displaced Mass Ratio

Mass ratio (equation 1.3) is the mass of material displaced by a crater of a given impact angle divided by the mass of material displaced by a vertical impact (at similar impact velocities). Mass ratio is plotted versus impact angle for both sets of experimental craters in Figure 3.23. Gault and Wedekind noted that their mass ratios are approximately proportional to the sine of the impact angle for craters into particulate materials, as shown by the $\sin\theta$ curves depicted in Figure 3.23.

Although there is some scatter in the data, the data points from my experiments done at lower velocities are overall higher than those done by Gault and Wedekind at higher velocities. However, when the velocity adjusted volumes for the low-velocity experiments (section 3.1.6 and Figure 3.1.6. 3) are used to compute the mass ratio, the data from the low-velocity experiments and the high-velocity experiments both seem to follow a $\sin\theta$ curve (Figure 3.24), with the exception of the very lowest impact angles.

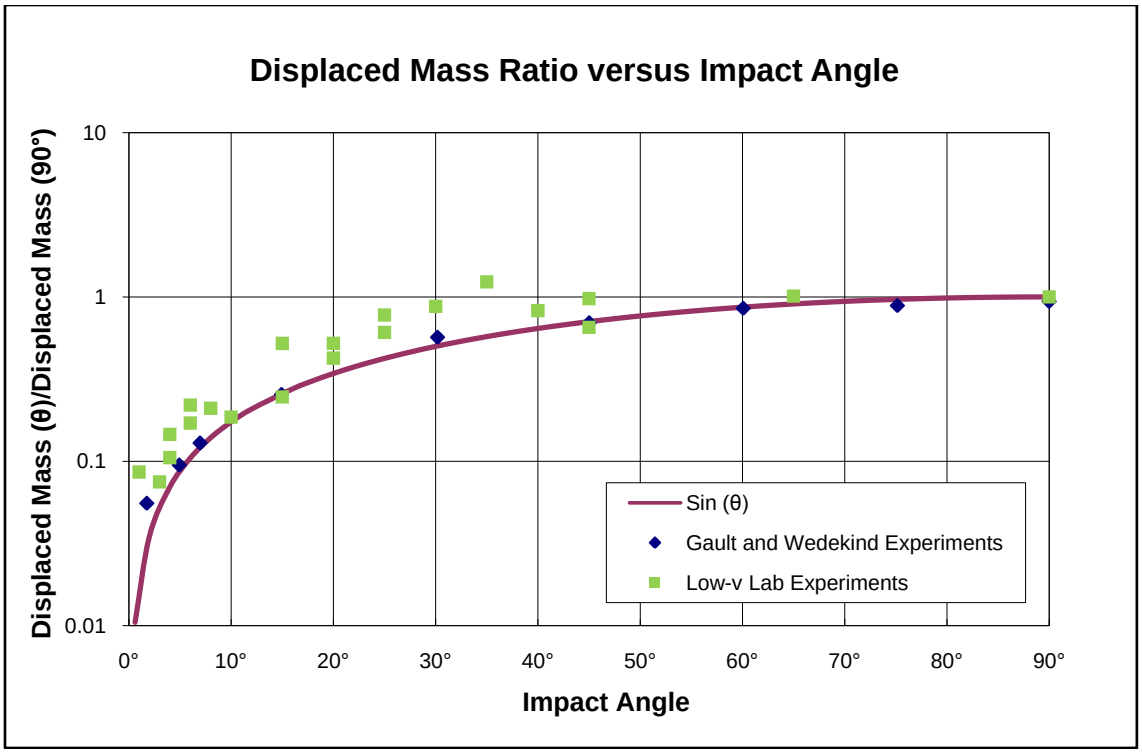

Figure 3.23. Displaced mass ratio versus impact angle. Quantities represented are the mass of material displaced by the impact (calculated using the volume of the impact crater and the density of the impact material), normalized by the mass of material displaced in a vertical impact. Blue Diamonds represent data from Gault and Wedekind (1978) Figure 8, aluminum and Pyrex projectiles into non-cohesive quartz sand (444 rounds, velocities = 1.8 – 6.8 km/sec). Green squares represent data from the low velocity lab experiments. The solid line represents the sine of the impact angle.

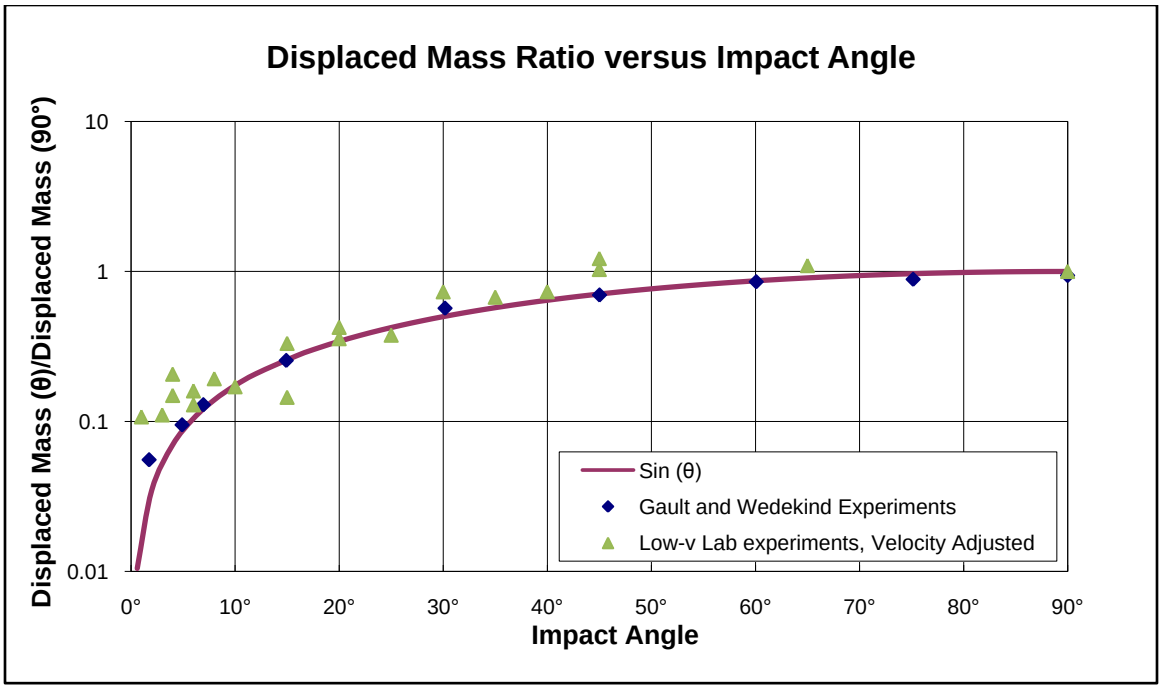

Figure 3.24. Velocity adjusted displaced mass ratio versus impact angle. Quantities represented are the mass of material displaced by the impact (calculated using the volume of the impact crater and the density of the impact material for the low-velocity experiment data), normalized by the mass of material displaced in a vertical impact. Blue Diamonds represent data from Gault and Wedekind (1978) Figure 8, Aluminum and Pyrex projectiles into non-cohesive quartz sand (444 rounds, velocities = 1.8 – 6.8 km/sec). Green triangles represent mass displaced data from the low velocity lab experiments, using the velocity adjusted volume values. The solid line represents the sine of the impact angle.

3.2.3 Crater Wall Slope

Gault and Wedekind only published what they termed ‘representative profiles’ of craters at a few impact angles (Figure 3.25). It is unclear if these are actual profiles of particular craters that were chosen to represent all craters at each angle, or if they are sketches that were drawn to represent the general geometry observed at each impact angle. I digitized these profiles and computed the slopes for the interior crater walls using the same methods as for the profiles collected at the low-velocity lab (discussed in section 3.1.4). The wall slopes for their experiments are plotted versus impact angle, along with the wall slopes from the low velocity experiments, in Figure 3.26. The wall slopes from the high velocity experiments differ from the low-velocity wall slopes in that the downrange wall is never steeper than the uprange wall; the uprange wall of the high-velocity craters is either steeper or the two walls have equal slopes. Overall, the slope values for the two sets of experiments are in the same range, with the exception of the uprange wall in the 5° impact angle crater from the high velocity craters, which is extremely steep.

It is difficult to know whether the differences seen in wall slopes between the two sets of experiments are due to the large difference in projectile velocity, or due to different target material properties. Unfortunately, the only crater profiles available for the high velocity craters being compared here were formed in pumice dust (not sand, as was used for all of the low-velocity experiments and much of the high velocity experiments). Gault and Wedekind note that while the quartz sand was “virtually cohesionless,” the pumice dust exhibited “some cohesion.” This may cause differences in

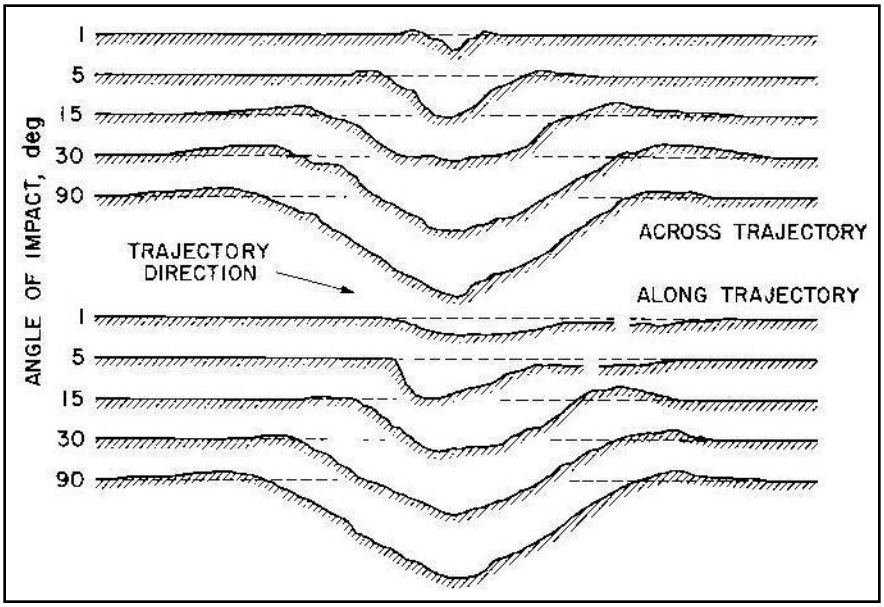

Figure 3.25. Geometry of craters formed in pumice dust by oblique impacts of pyrex spheres at velocities of ~ 6.4 km/sec. (fig. 5, from Gault and Wedekind, 1978).

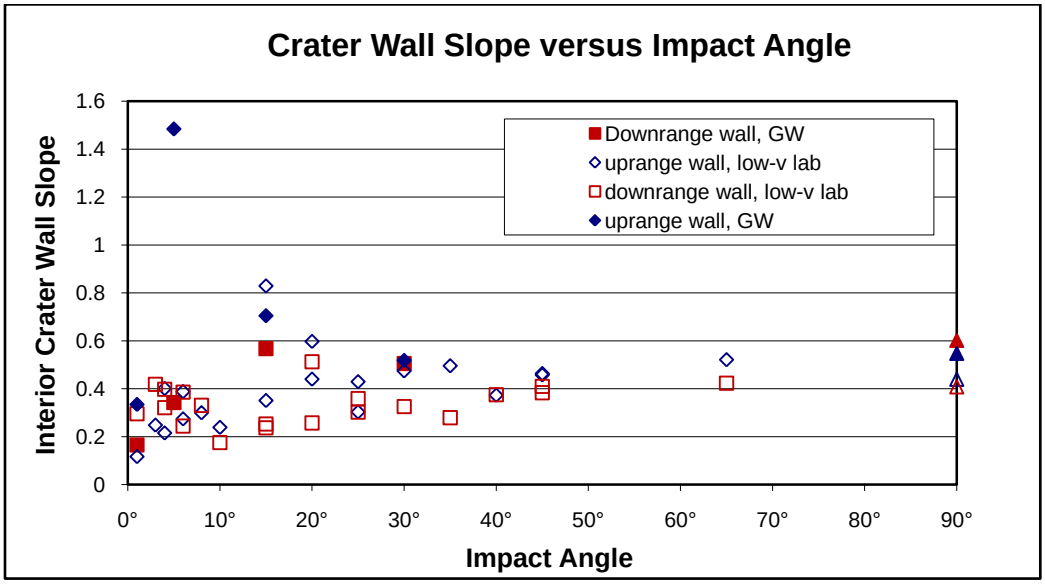

Figure 3.26. Interior crater wall slope versus impact angle. Closed symbols represent data from Gault and Wedekind, while open symbols represent my experiments in the low-velocity lab. Blue diamonds represent slopes for the uprange wall of each crater. Red squares represent the downrange wall. The craters at 90° (vertical), by definition, do not have an uprange or downrange wall. However, slopes of two opposing walls for these craters were calculated, and are plotted in the graph (triangles).

the resultant crater shape due to the grains of sand sliding along the surface more, but I do not believe that it would be responsible for steeper walls in the lower-cohesion material (sand, low-velocity experiments).

The steep downrange wall in the low-velocity impacts may be due to the projectile mounding up target material in front, and not transferring enough momentum to the target in order to eject material ballistacally out of the crater. The shallow downrange wall in the high-velocity craters is likely due to the downrange target material being ejected (not pushed forward). This may account for the differences seen in the crater shape between the sets of experiments. However, it is difficult to know how much of an affect the small differences in target materials may have without being able to conduct experiments with exactly the same target materials.

3.2.4 Depth to Diameter Ratio

Gault and Wedekind published their depth to diameter ratios using apparent depths and diameters. Where craters depart from circular, they used the average diameter, D_{avg}:

$$D_{avg} = ½ (D_{max} + D_{min}) \quad (3.6)$$

where D_{max} and D_{min} are the maximum and minimum apparent crater diameters. According to equation 3.5, depth to diameter ratios calculated using apparent diameters are not comparable to those with rim-to-rim measurements. Therefore Figure 3.27 shows apparent depth to diameter ratio versus impact angle for both sets of experimental data. Red open squares represent data from my low-velocity experiments. Yellow

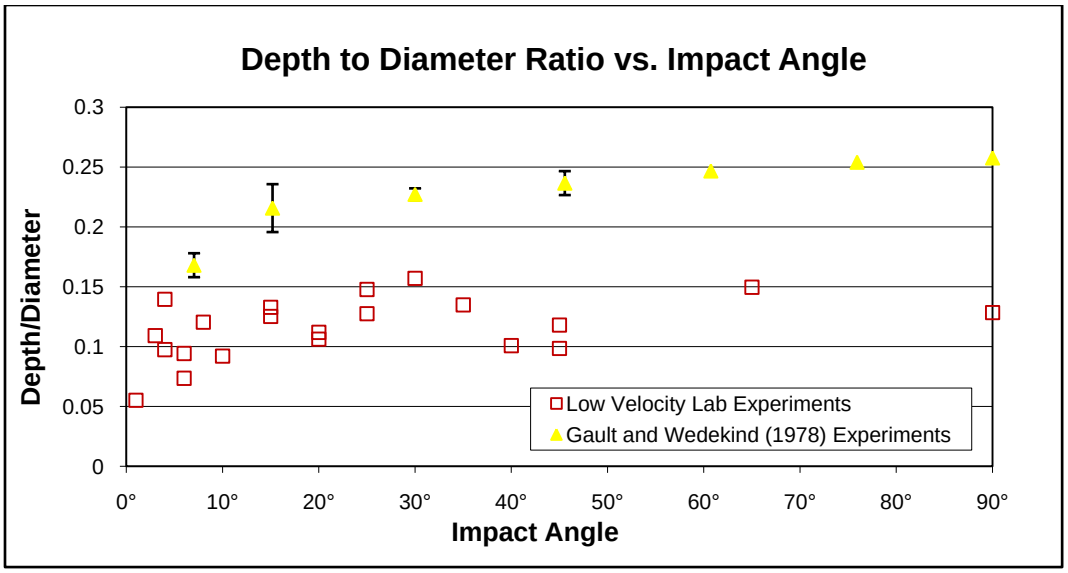

Figure 3.27. Depth to diameter ratio versus impact angle. Red open squares represent data from my low-velocity experiments. Yellow triangles represent points from Gault and Wedekind's experiemnts. These eight data points represent 121 rounds fired into quartz sand with velocities of 3.6-7.2 km/sec. Error bars are standard deviations, as reported by Gault and Wedekind (error bars are smaller than the data point symbol for their higher angle data points). Both data sets use apparent depth and average apparent diameter (measured with respect to the pre-impact surface).

triangles represent points from Gault and Wedekind's impacts. Although a large amount of scatter is present in the data from the low-velocity experiments, it is apparent that these depth to diameter ratios are lower than those of Gault and Wedekind.

A close examination of the profiles for the higher impact angle craters for both sets of experiments (Figures 3.9, 3.10, and 3.25) reveals a difference in the shape of the crater floors. The higher angle craters in the Gault and Wedekind experiments (30° and 90°) have cone shaped crater profiles, while the craters from the low-velocity experiments have relatively flat floors. The flat floors could be a result of the fate of the projectile. Gault and Wedekind (1978) state that, for their experiments, "projectile material is always ejected during an impact event either as a solid, or in the liquidous or vaporous state." In contrast, the projectiles in the low velocity experiments were never broken or damaged during impact, and remained in the crater for near-vertical impacts.

It is possible that the low-velocity craters were initially cone shaped, and then the craters were filled in slightly by wall slumping or material falling in, causing the floors to become flat. This effect would be more pronounced in the craters formed in sand, a nearly cohesionless material (as compared to the pumice, as discussed in section 3.2.3). This would mean that the original craters were deeper, and the depth to diameter ratios would have been higher for these craters. Increasing the depths for the higher angle impacts would make a more consistent trend for the low-velocity experiments, but the ratios would likely still be lower than the data from Gault and Wedekind.

3.2.5 Ejecta Distribution

Gault and Wedekind analyzed the images of their experimental craters formed in pumice dust (Figures 1.1 and 1.2) to see how ejecta distribution changes with impact angle. They found that crater ejecta remains symmetric around the crater down to impact angles of about 45°. At around 45°, the ejecta becomes visibly asymmetric. At approximately 20°, a clear uprange forbidden zone develops that extends to the crater wall. Below 20°, decreasing amounts of ejecta are present in the downrange direction until a second forbidden zone develops around 5°, creating a 'butterfly' ejecta pattern.

Comparing the results of the high velocity experiments of Gault and Wedekind to my low-velocity experiments highlights several important differences in ejecta distribution (see Table 3.2 for a summary). In the low-velocity experiments, asymmetric ejecta is present at higher impact angles; asymmetry occurs when impact angles reach 60°, compared to 45° in the high velocity experiments. It is possible, however, that Gault and Wedekind may have seen asymmetric ejecta if they had performed experiments at angles between 60° and 45° (which they did not). Presence of an uprange forbidden zone occurs at the same impact angle (20°) in both sets of experiments. The most striking difference between the two sets of experiments is the complete lack of a downrange forbidden zone in all of the low-velocity experiments. A second forbidden zone ('butterfly' ejecta pattern) is seen in the high velocity experiments at impact angles of around 5° and lower, but is never seen in the low-velocity experiments.

Table 3.2. Comparison of ejecta distribution for both sets of experiments. Impact angle ranges given are the approximate ranges where ejecta of a certain ejecta pattern is present.

COMPARISON OF EJECTA DISTRIBUTION		
Ejecta Pattern	**Low Velocity Experiments**	**High Velocity Experiments**
Symmetric	$\theta > 60°$	$\theta > 45°$
Asymmetric	$60° > \theta > 20°$	$45° > \theta > 20°$
Uprange Forbidden Zone	$20° > \theta$	$20° > \theta > 5°$
'Butterfly' (uprange and downrange forbidden zones)	Not seen	$5° > \theta$

4. Conclusions.

Low velocity experimentation has shown that craters are circular for impact angles ranging from vertical to ~15°. Below 15°, craters become increasingly more elliptical as impact angle decreases. Crater depth, diameter, and volume all generally decrease as impact angle decreases from vertical to horizontal. However a marked change in data trend and value occurs at or near impact angles of 35° for depth, diameter, and volume (not elongation). Onset of wall slumping at a particular impact angle is not thought to be the cause for the noted change at 35°.

Crater volumes were calculated using two methods: one assuming an elliptical paraboloid shape, and the other integrating along vertical profiles. For most craters the two volumes are nearly the same, suggesting that the craters *are* roughly shaped like elliptical paraboloids, even for the very low angle impacts. This result may be of interest to future researchers because it is likely unnecessary to resort to more involved methods for determining volume.

When comparing the crater shapes (wall slopes) of the high and low velocity craters, there is a marked difference in the lowest angle impacts; the low velocity craters have downrange walls that are steeper than the uprange walls. The steep downrange wall in the low-velocity impacts may be due to the projectile mounding up target material in front, and not transferring enough momentum to the target to eject material ballistacally out of the crater. The shallow downrange wall in the high-velocity craters is likely due to the downrange target material being ejected (and not simply pushed forward).

In the low-velocity experiments, asymmetric ejecta is present at higher impact angles; onset of asymmetry occurs when impact angles reach 60°, compared to 45° in the high velocity experiments. Presence of an uprange forbidden zone occurs at the same impact angle (20°) in both sets of experiments. The most striking difference between the two sets of experiments is the complete lack of a downrange forbidden zone in all of the low-velocity experiments. A second forbidden zone is seen in the high velocity experiments at impact angles of around 5° and lower, but is never seen in the low-velocity experiments.

With the exception of the very lowest impact angles, the low-velocity oblique impact experiments presented here yield similar changes in crater characteristics with varying impact angles to the previous high-velocity experiments of Gault and Wedekind (1978). The differences observed in the lowest angle impacts may be useful in distinguishing between primary and secondary low angle impact craters. Excluding deceleration due to an atmosphere, primary impactors must impact the surface at or above planetary escape velocity, while secondary impacts occur at less than escape velocity. None of my highly oblique low velocity experiments yielded downrange forbidden zones, while the high velocity experiments of Gault and Wedekind did. This implies that the presence or absence of a downrange forbidden zone may be a useful indicator in differentiating between primary and secondary planetary impact craters, particularly if the impact angle can be estimated by an independent method

5. References

Barlow, N. G. and C. B. Perez, Martian impact crater ejecta morphologies as indicators of the distribution of subsurface volatiles, JGR, 108(E8), 5085, 2003.

Bottke, W. F., S. G. Love, D. Tytell, and T. Glotch, Interpreting the Elliptical Crater Populations on Mars, Venus and the Moon. *Icarus*, 145, 108-121, 2000.

Chappelow, J. E. and R. R. Herrick, On the Origin of a Double, Oblique Impact on Mars. *Icarus,* in press.

Gault, D. E. and J. A. Wedekind, Experimental Studies of Oblique Impact, *Proc. lunar. Planet. Sci. Conf. 9th*, 3843-3875, 1978.

Hartmann, W. K., Martian cratering VI: Crater count isochrons and evidence for recent volcanism from Mars Global Surveyor, *Meteorit. Planet Sci*., 34, 167-177, 1999.

Herrick, R. R. and N. K. Forsberg-Taylor, The shape and appearance of craters formed by oblique impact on the Moon and Venus, *Meteorit. Planet Sci*., 38(11), 1551-1578, 2003.

Herrick, R. R. and K. K. Hessen, The Planforms of low-angle impact craters in the northern hemisphere of Mars, *Meteorit. Planet Sci*., 41(10), 1483-1495, 2006.

Melosh, H. J., Ejection of rock fragments from planetary bodies, *Geology*, 13(2), 144-148, 1985.

Melosh, H. J., *Impact Cratering, A Geologic Process,* Oxford University Press, New York, New York, USA, 1989.

Schultz, P. H. and A. B. Lutz-Garihan, Grazing Impacts on Mars: A Record of Lost Satellites, *JGR*, 87, Supplement, A84-A96, 1982.

Shoemaker, E. M., Interpretation of lunar craters, in *Physics and Astronomy of the Moon* (Z. Kopal, Ed.), pp 283-351. Academic Press, New York, 1962.

Yamamoto, S., K. Wada, N. Okabe, and T. Matsui, Transient crater growth in granular targets: An experimental study of low velocity impacts into glass sphere targets. *Icarus*, 183, 215-224, 2006.

8. Appendix

The following contains one image from each impact crater in the low-velocity experiments that were used in the preceding analysis. Red laser lines, where visible, are approximately perpendicular to the projectile direction. For all craters (except those with vertical impact angles), the projectile trajectory is from the top to the bottom of the page. Images of the craters can also be found in the attached disc.

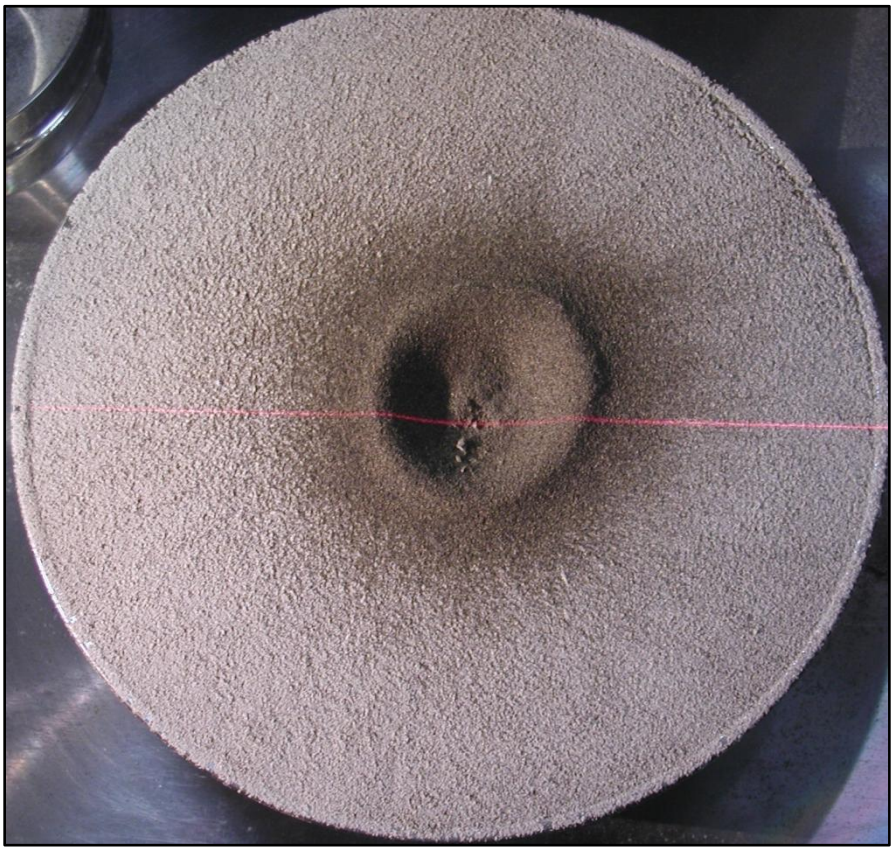

Figure A.1. Image of crater with 90° impact angle and projectile velocity of 181 m/s.

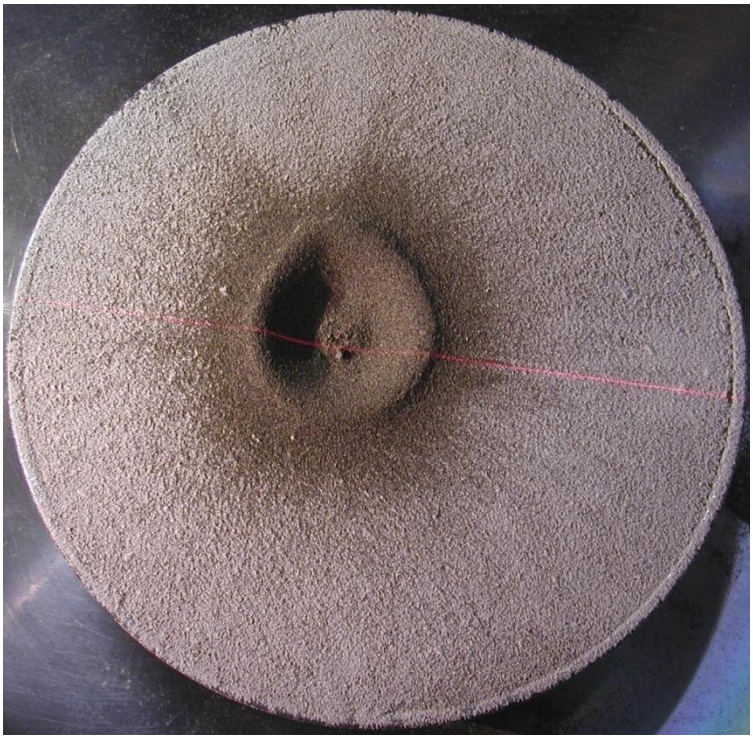

Figure A.2. Image of crater with 90° impact angle and projectile velocity of 179 m/s.

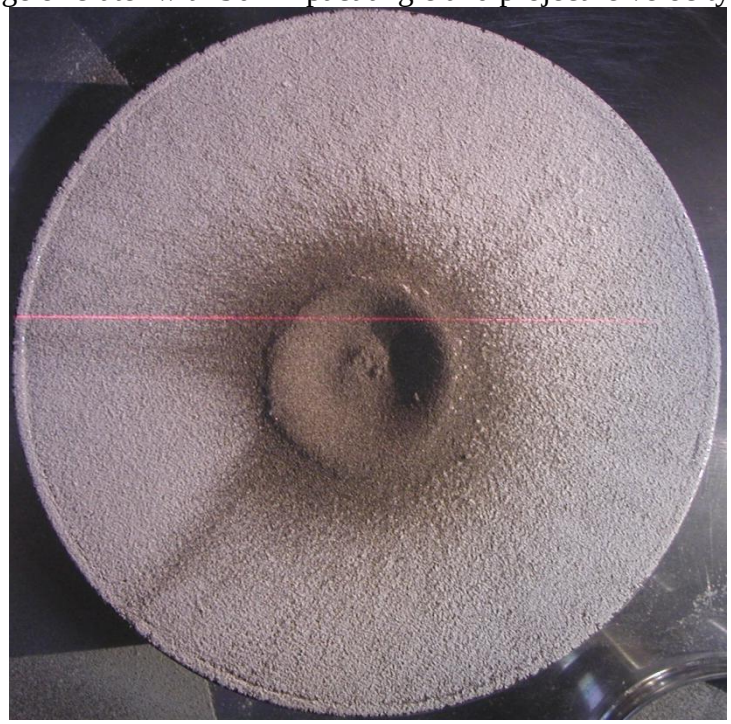

Figure A.3. Image of crater with 75° impact angle and projectile velocity of 162 m/s.

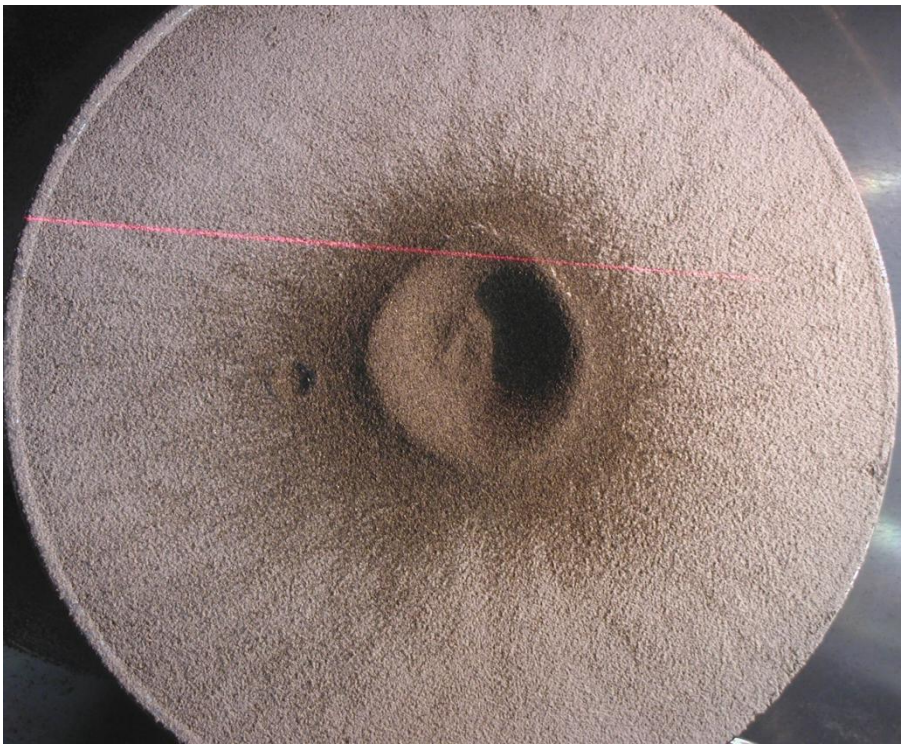

Figure A.4. Image of crater with 65° impact angle and projectile velocity of 174 m/s.

Figure A.5. Image of crater with 60° impact angle and projectile velocity of 176 m/s.

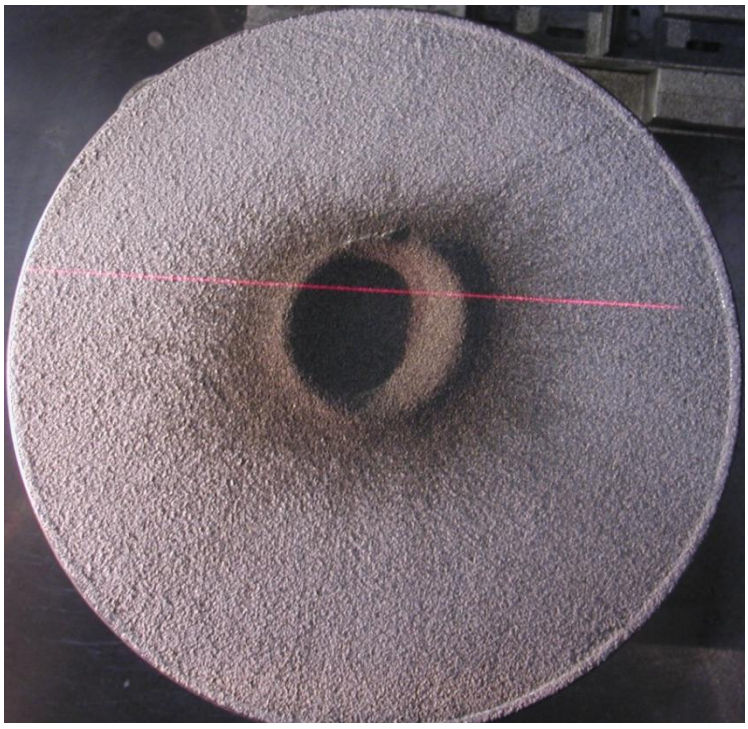

Figure A.6. Image of crater with 50° impact angle and projectile velocity of 216 m/s.

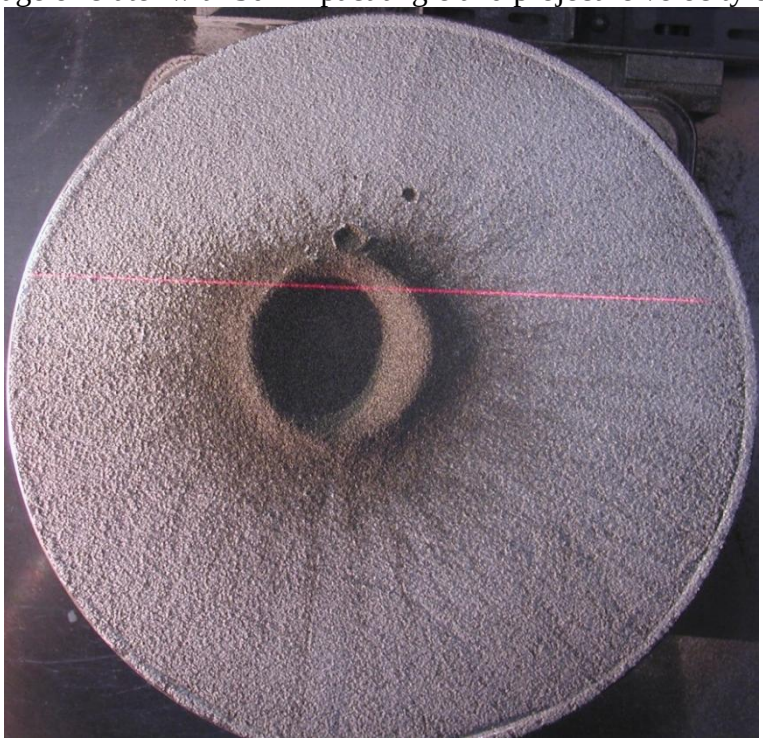

Figure A.7. Image of crater with 45° impact angle and projectile velocity of 205 m/s.

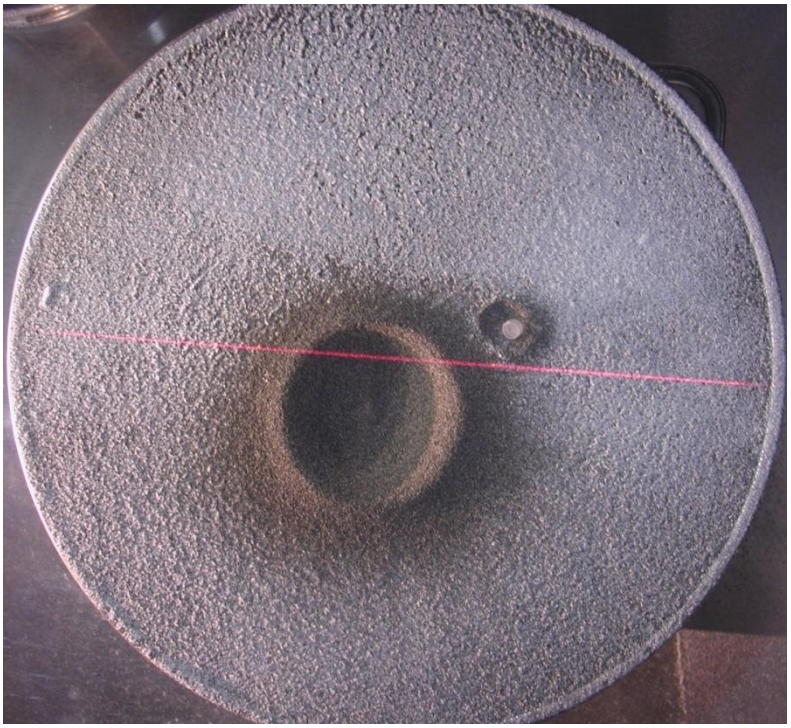

Figure A.8. Image of crater with 45° impact angle and projectile velocity of 162 m/s.

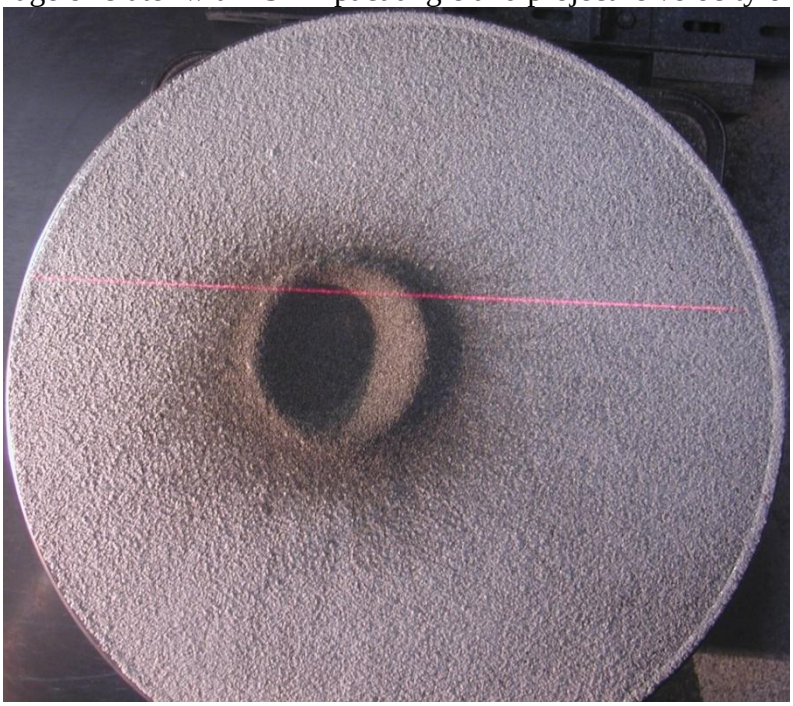

Figure A.9. Image of crater with 45° impact angle and projectile velocity of 144 m/s.

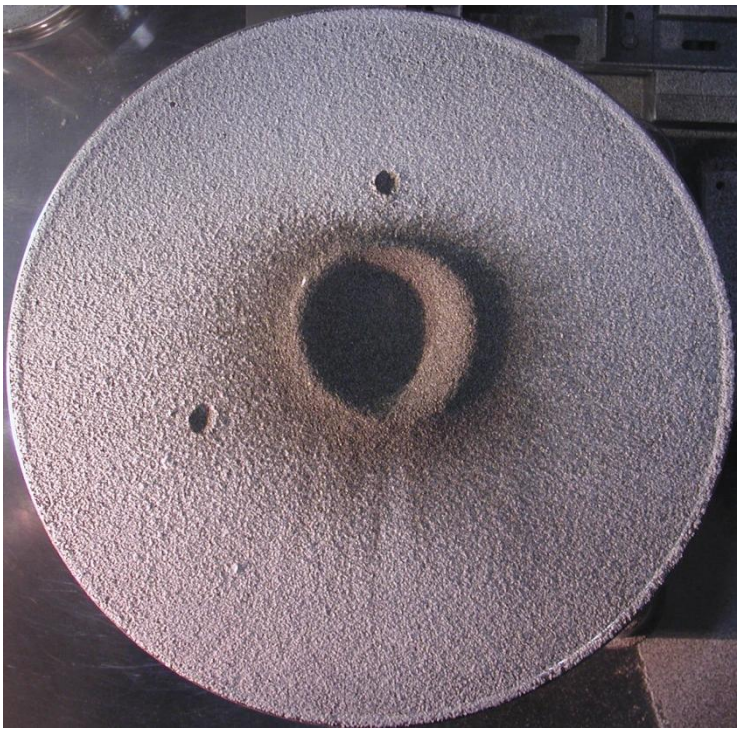

Figure A.10. Image of crater with 40° impact angle and projectile velocity of 192 m/s.

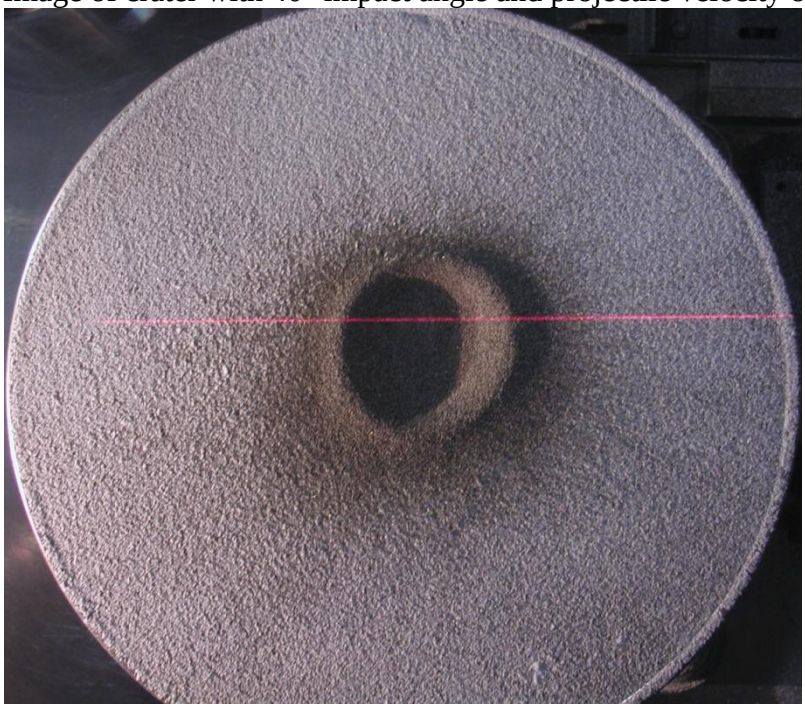

Figure A.11. Image of crater with 40° impact angle and projectile velocity of 151 m/s.

Figure A.12. Image of crater with 35° impact angle and projectile velocity of 245 m/s.

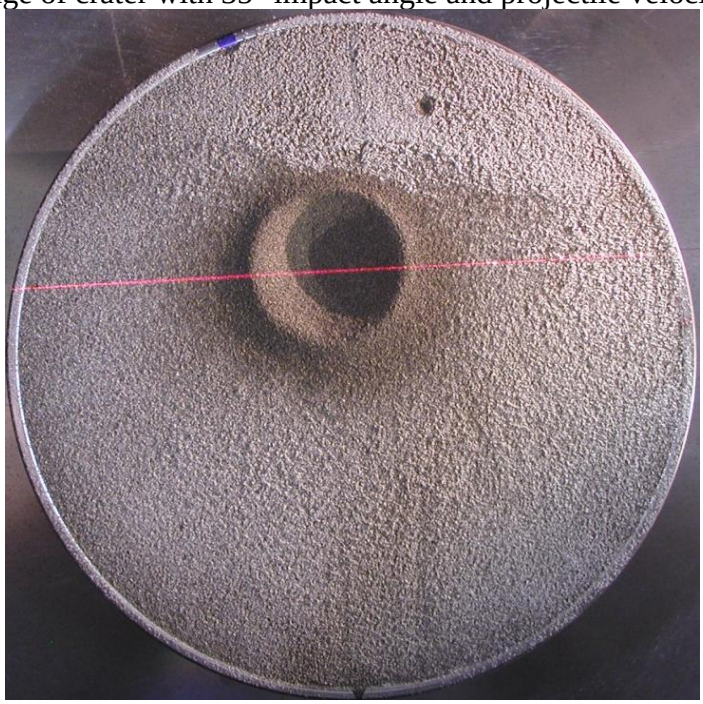

Figure A.13. Image of crater with 30° impact angle and projectile velocity of 198 m/s.

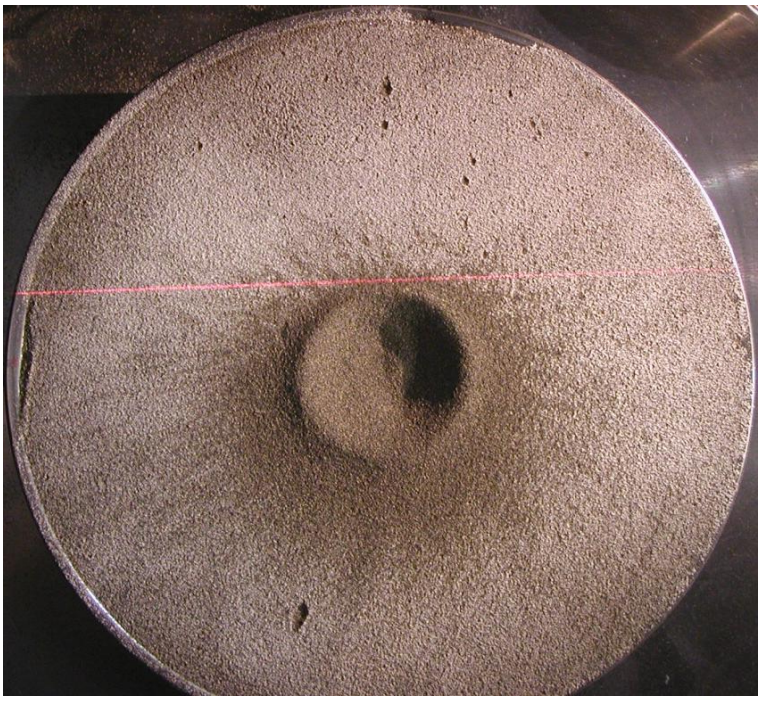

Figure A.14. Image of crater with 25° impact angle and projectile velocity of 260 m/s.

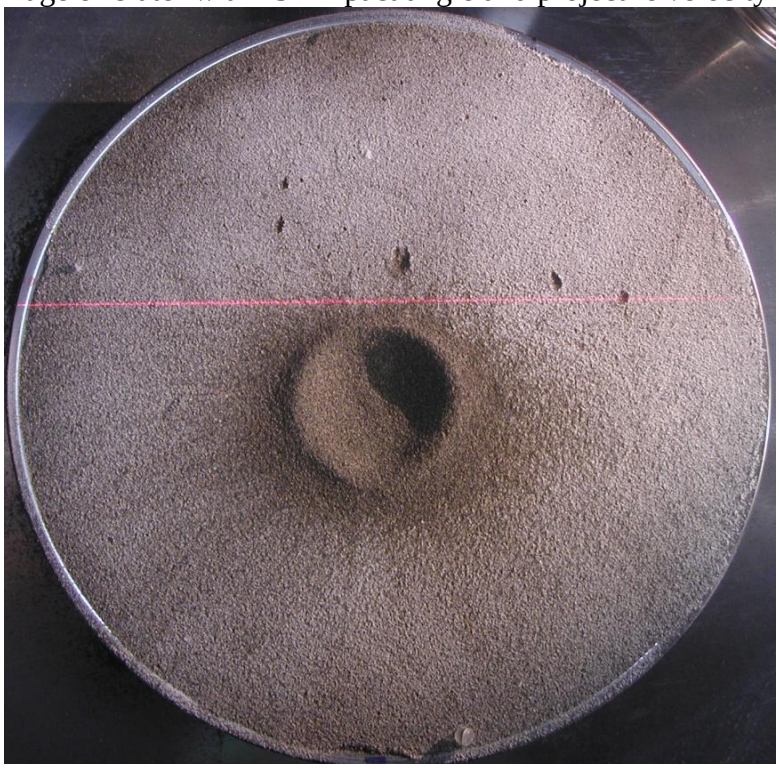

Figure A.15. Image of crater with 25° impact angle and an unknown projectile velocity.

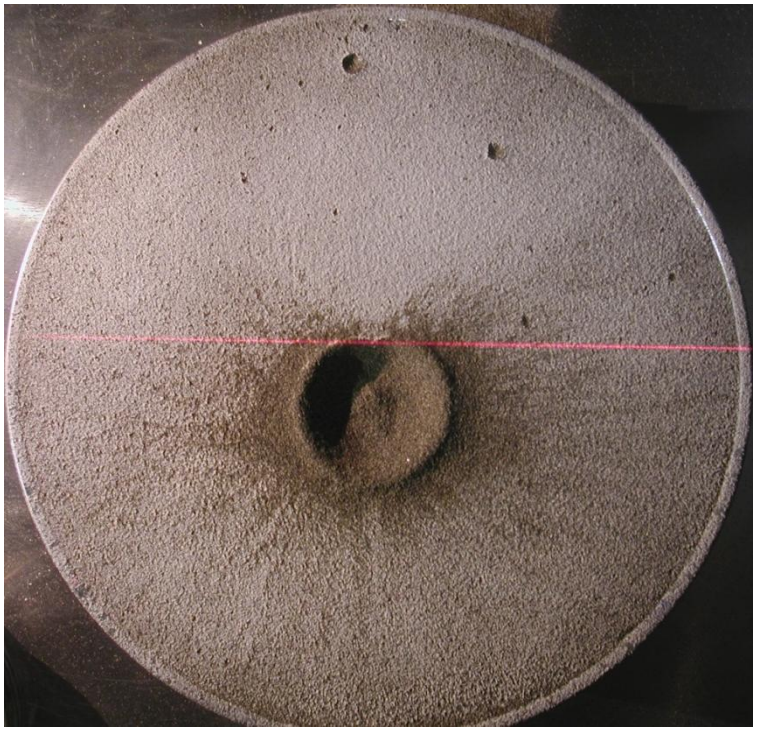

Figure A.16. Image of crater with 20° impact angle and projectile velocity of 219 m/s.

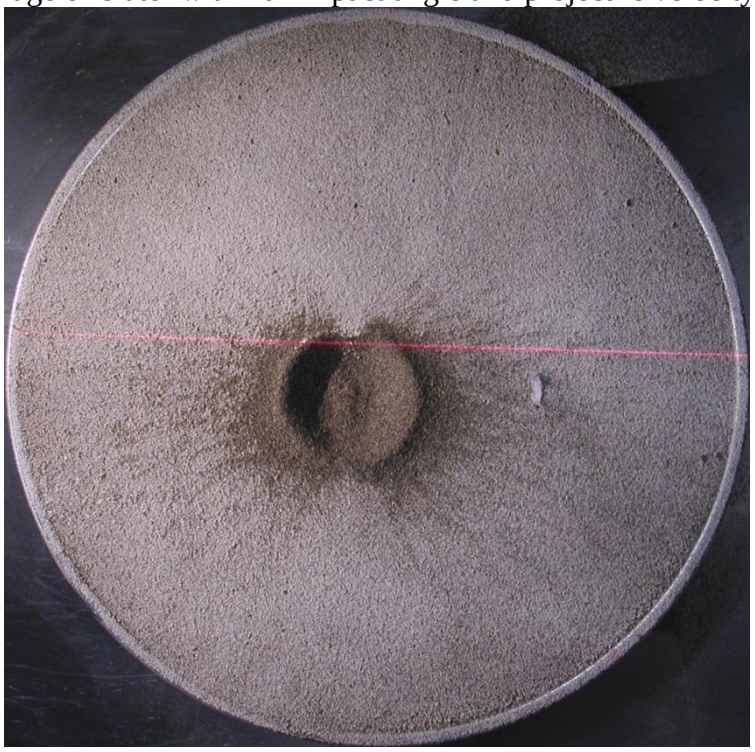

Figure A.17. Image of crater with 20° impact angle and projectile velocity of 181 m/s.

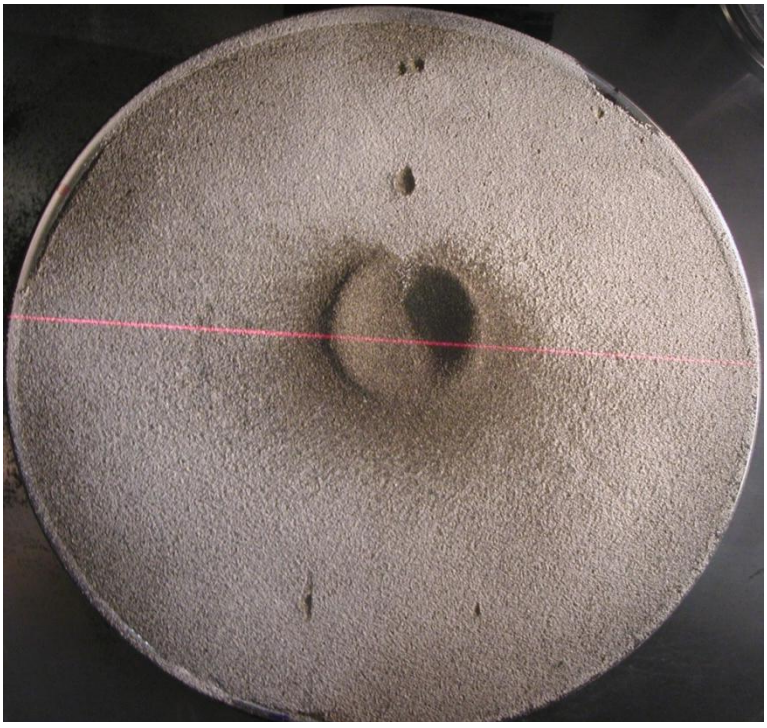

Figure A.18. Image of crater with 15° impact angle and projectile velocity of 227 m/s.

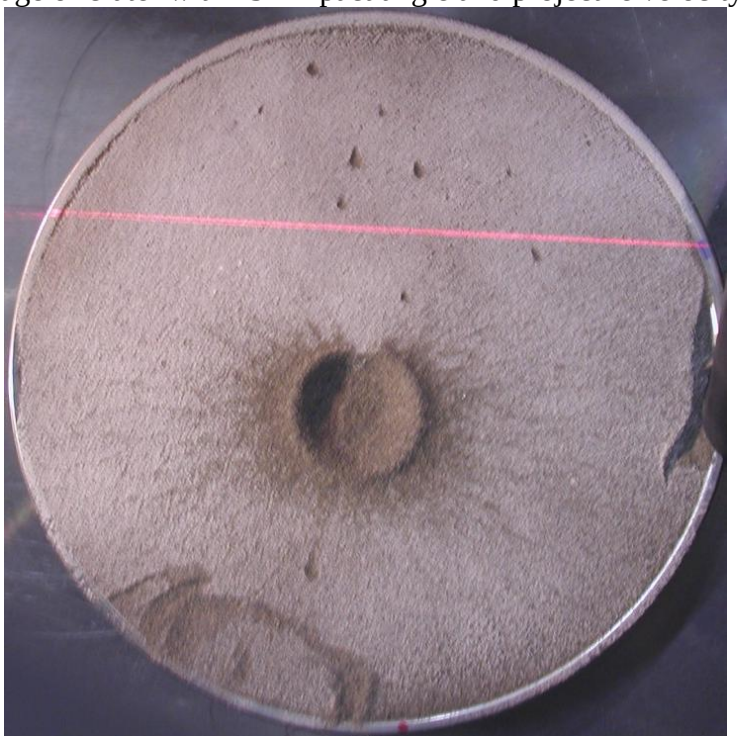

Figure A.19. Image of crater with 15° impact angle and projectile velocity of 236 m/s.

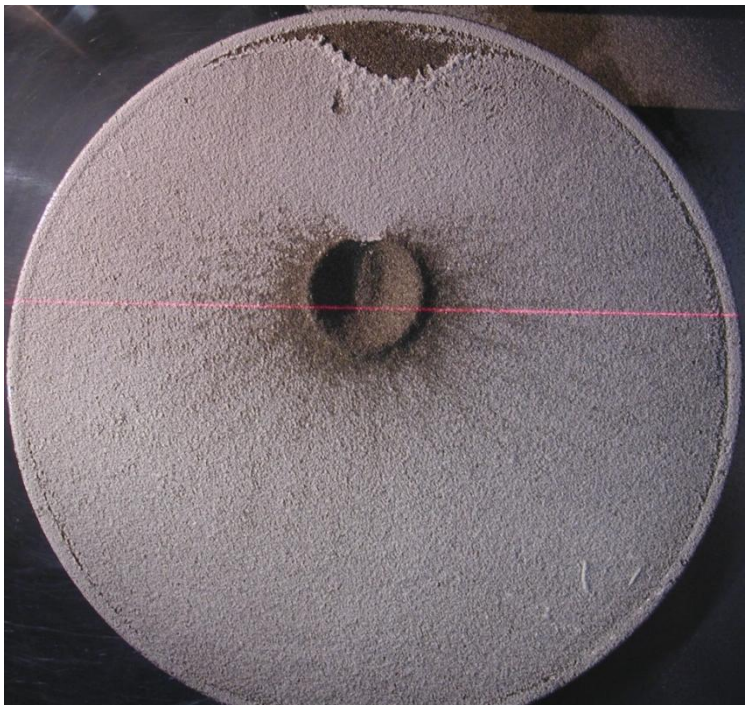

Figure A.20. Image of crater with 10° impact angle and projectile velocity of 156 m/s.

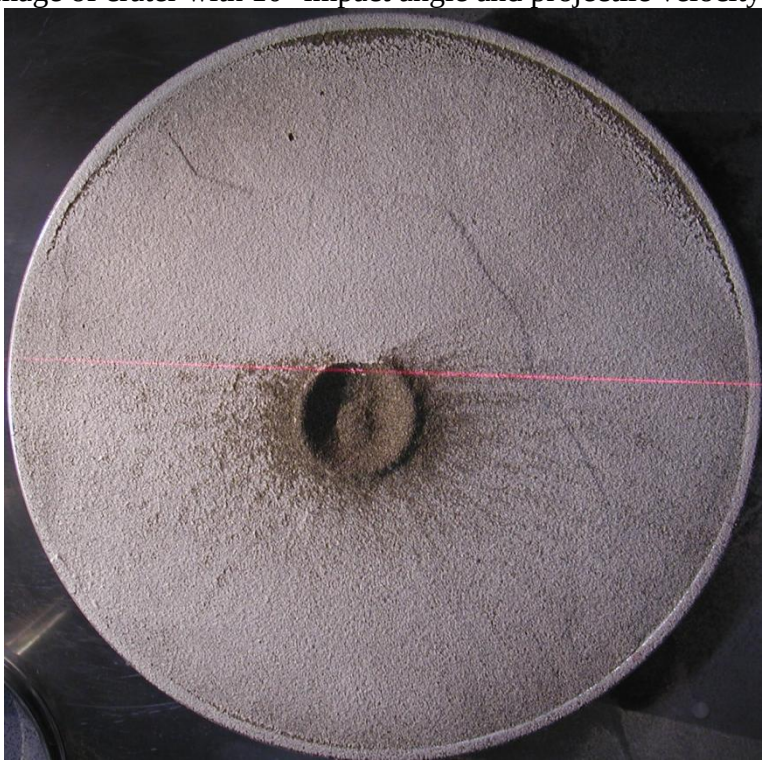

Figure A.21. Image of crater with 10° impact angle and projectile velocity of 189 m/s.

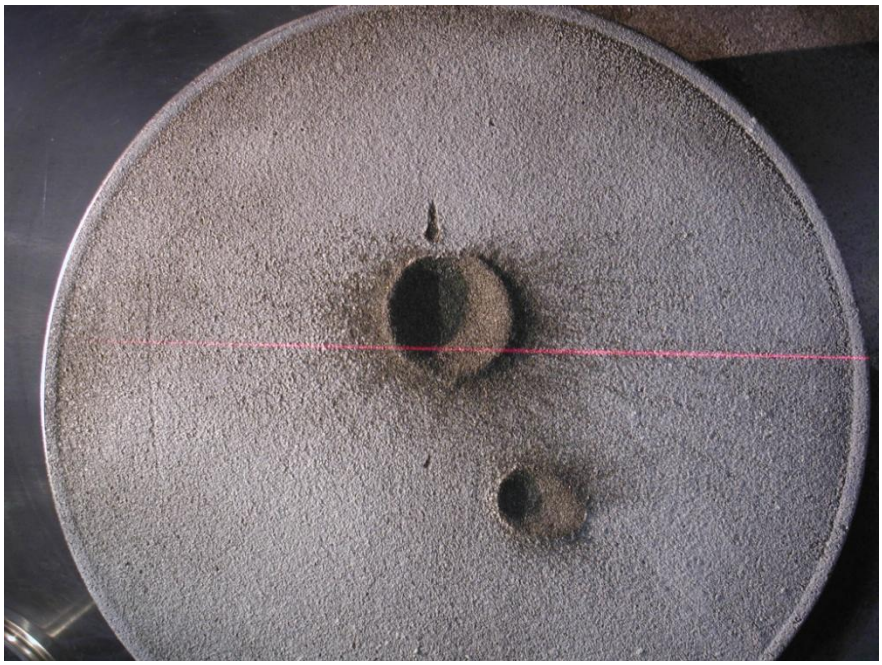

Figure A.22. Image of crater with 8° impact angle and projectile velocity of 179 m/s.

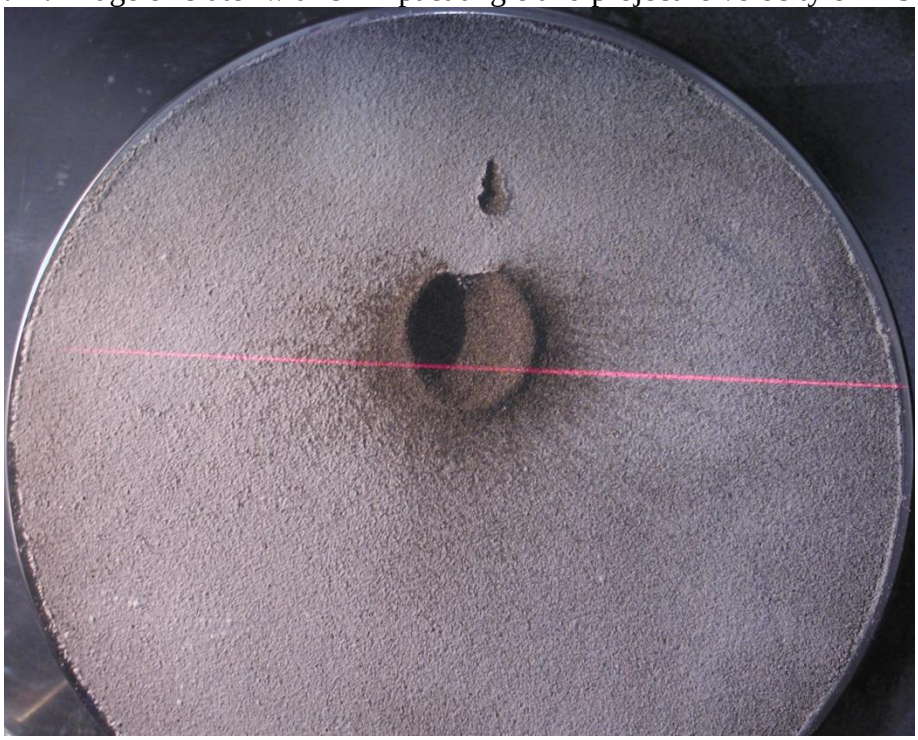

Figure A.23. Image of crater with 8° impact angle and projectile velocity of 189 m/s.

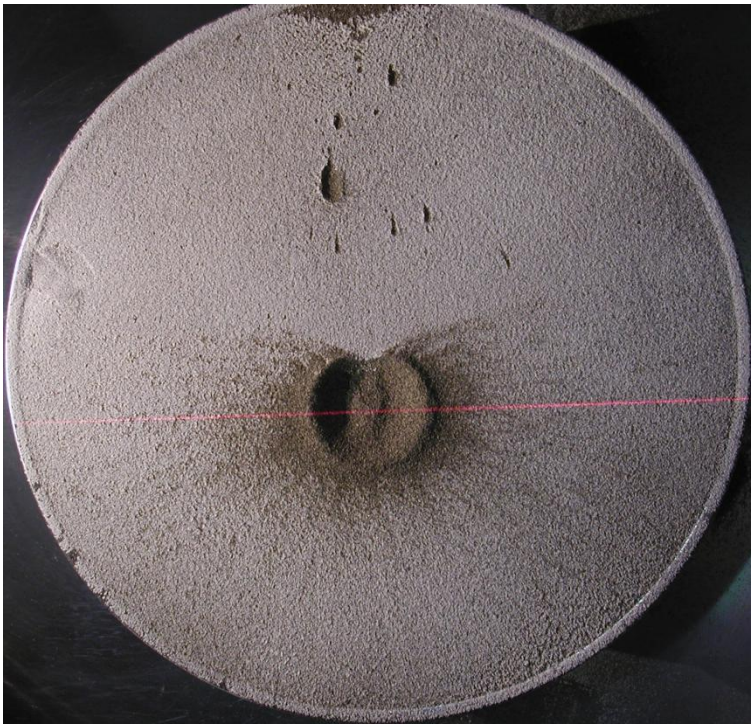

Figure A.24. Image of crater with 6° impact angle and projectile velocity of 236 m/s.

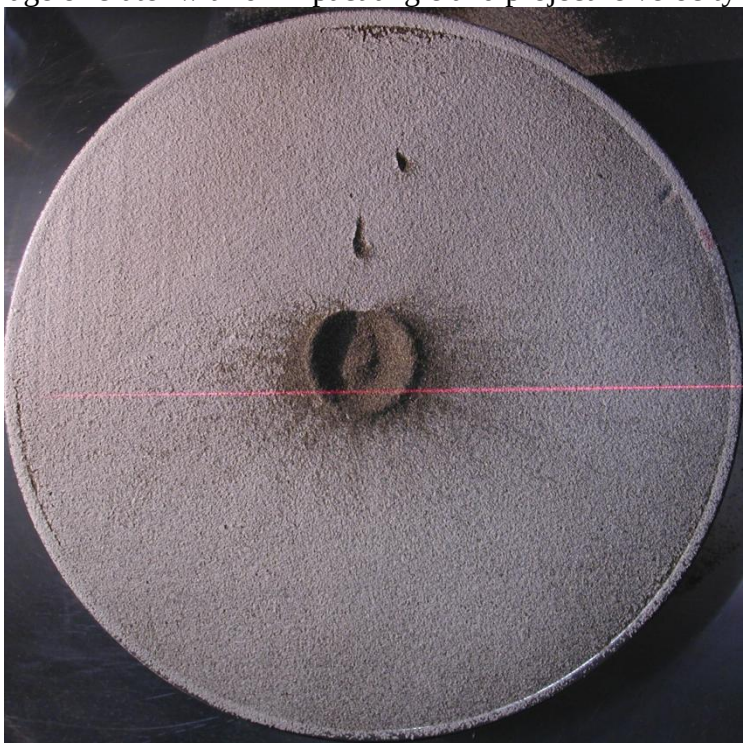

Figure A.25. Image of crater with 6° impact angle and projectile velocity of 187 m/s.

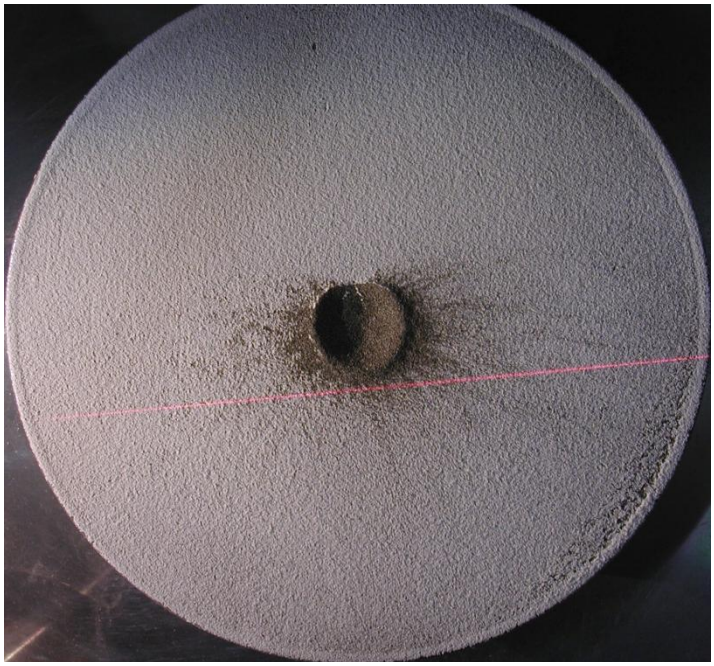

Figure A.26. Image of crater with 4° impact angle and projectile velocity of 152 m/s. Maximum diameter of 55 mm.

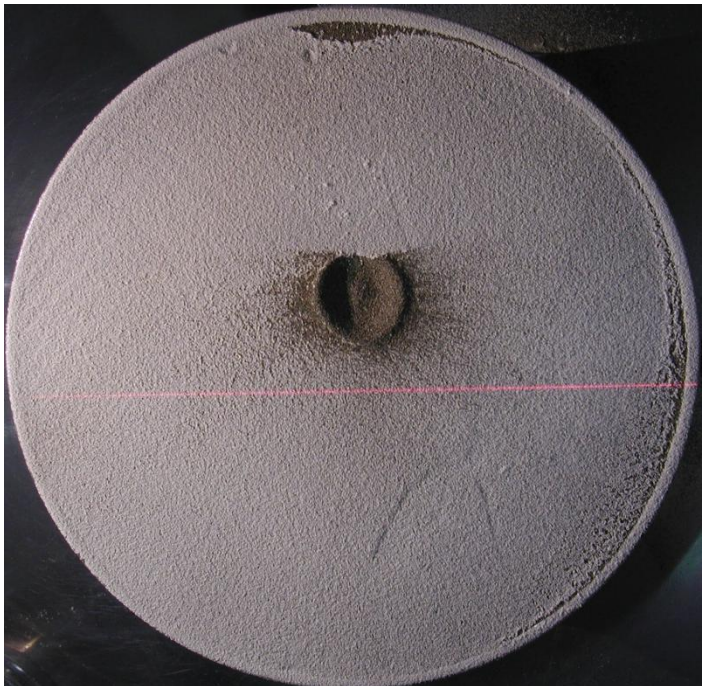

Figure A.27. Image of crater with 4° impact angle and projectile velocity of 152 m/s. Maximum diameter of 51 mm.

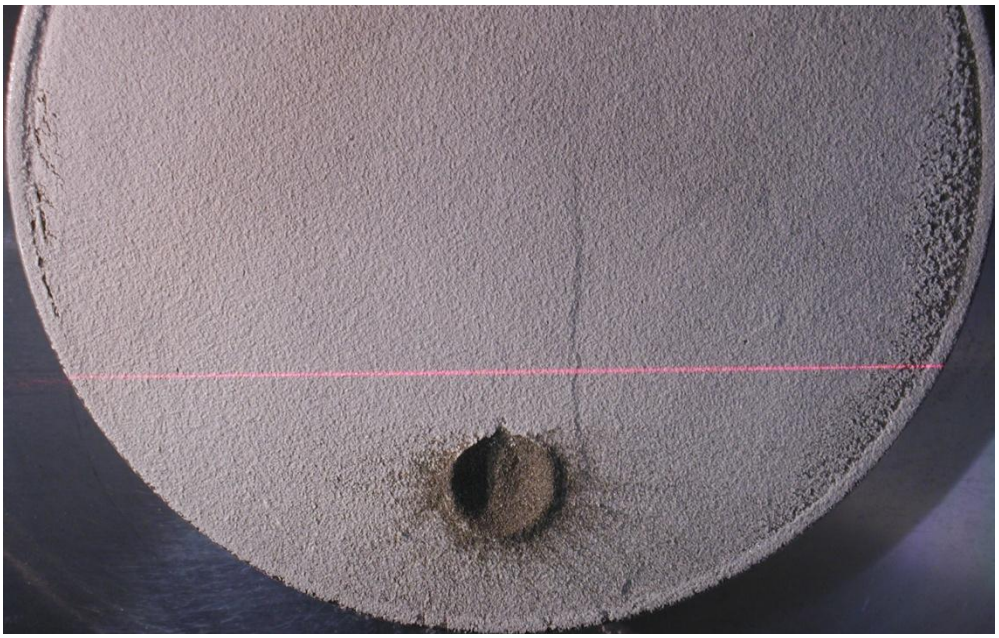

Figure A.28. Image of crater with 3° impact angle and projectile velocity of 149 m/s.

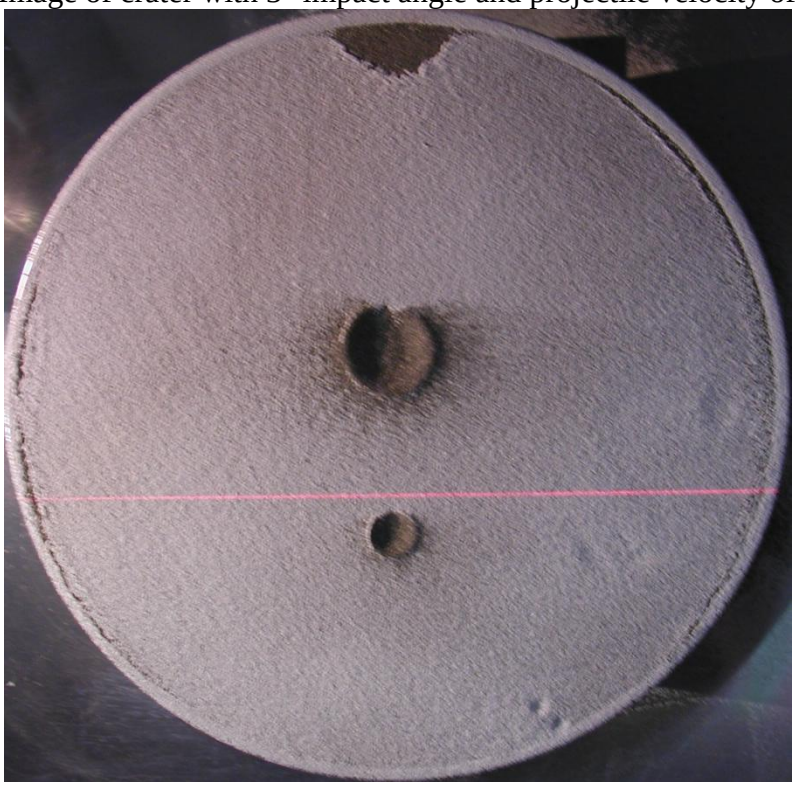

Figure A.29. Image of crater with 3° impact angle and projectile velocity of 152 m/s.

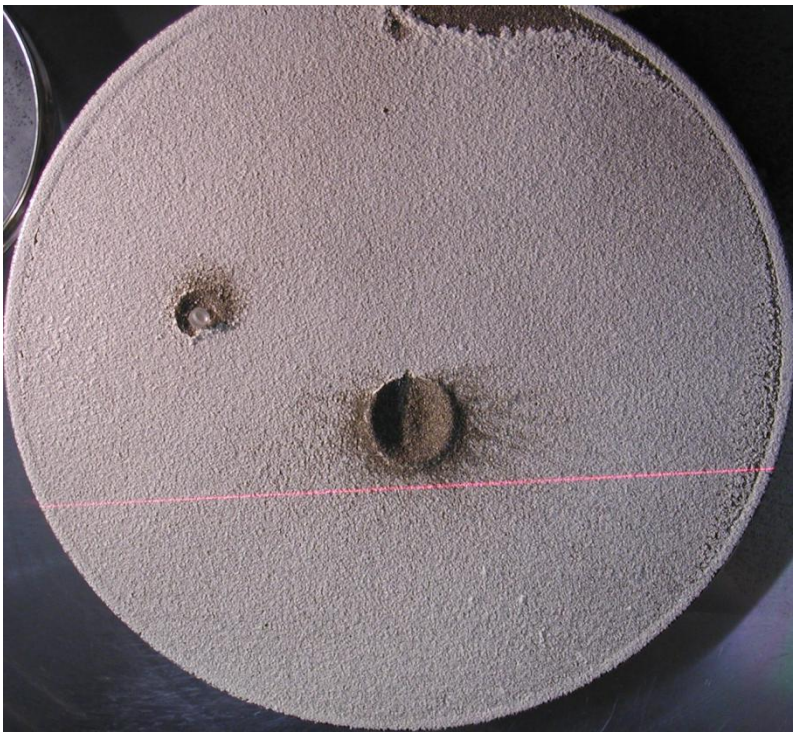

Figure A.30. Image of crater with 2° impact angle and projectile velocity of 171 m/s.

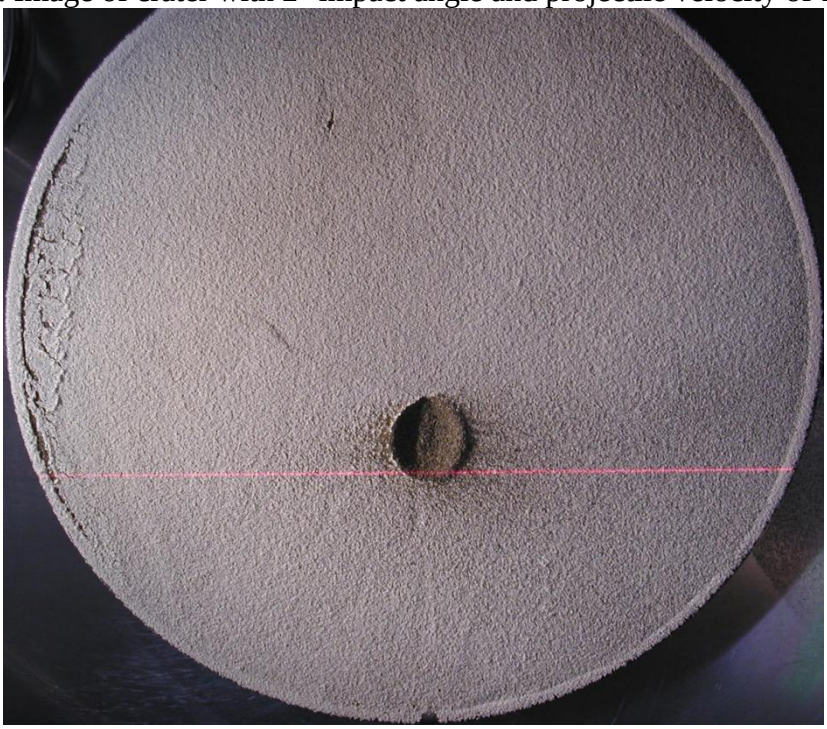

Figure A.31. Image of crater with 2° impact angle and projectile velocity of 154 m/s.

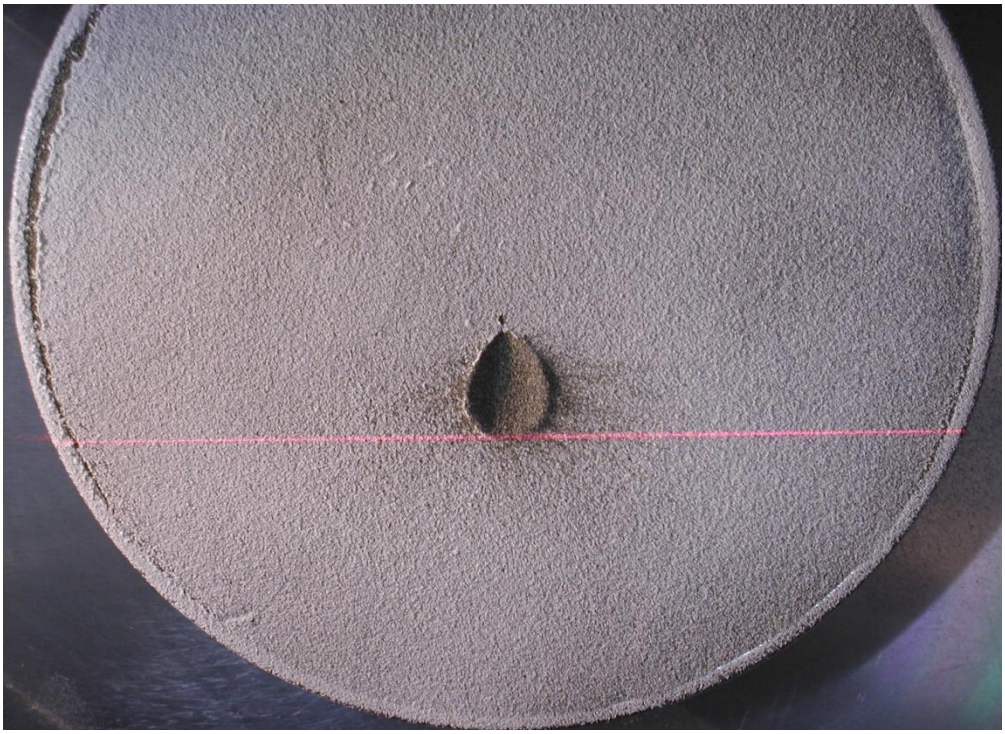

Figure A.32. Image of crater with 1° impact angle and projectile velocity of 176 m/s.

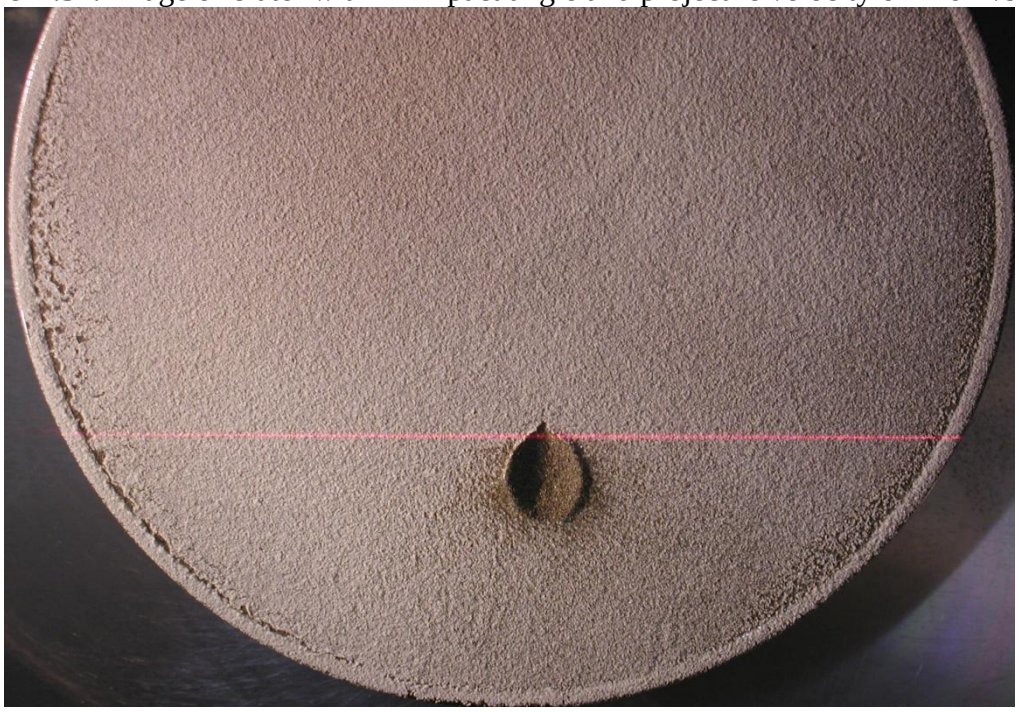

Figure A.33. Image of crater with 1° impact angle and projectile velocity of 162 m/s.

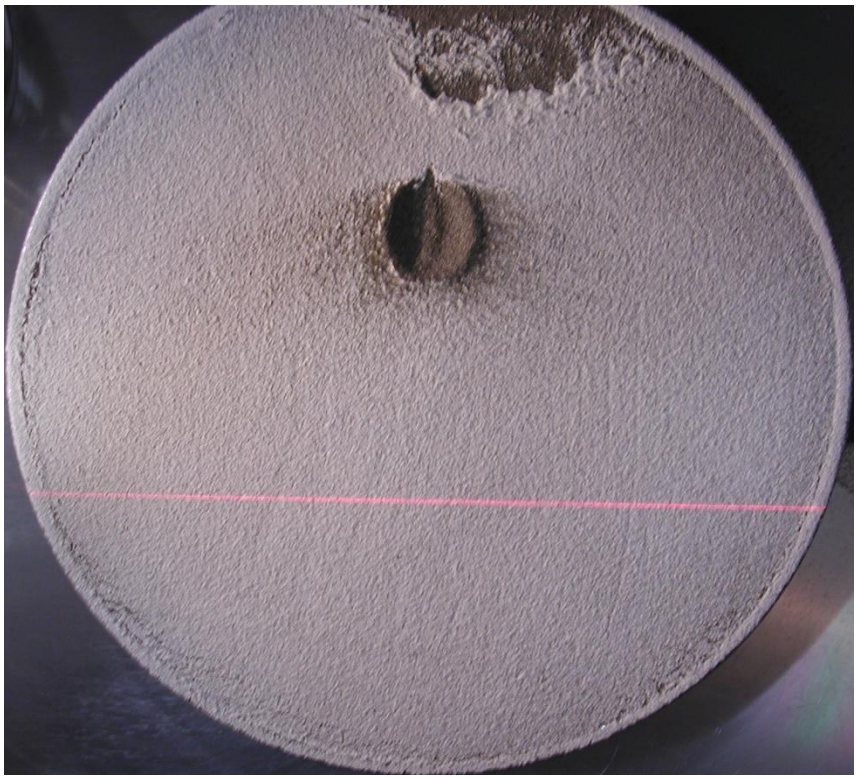

Figure A.34. Image of crater with 0.5° impact angle and projectile velocity of 167 m/s.